Geological Magazine

www.cambridge.org/geo

Age and petrogenesis of mafic granulites from central Madurai block, south India: implications on regional tectonics

J Amal Dev[1], JK Tomson[1], T Vijaya Kumar[2] and Nilanjana Sorcar[1]

[1]Solid Earth Research Group, National Centre for Earth Science Studies, Thiruvananthapuram, India and [2]Council of Scientific and Industrial Research – National Geophysical Research Institute, Hyderabad, India

Original Article

Cite this article: Dev JA, Tomson JK, Vijaya Kumar T, and Sorcar N (2023) Age and petrogenesis of mafic granulites from central Madurai block, south India: implications on regional tectonics. *Geological Magazine* **160**: 955–971. https://doi.org/10.1017/S0016756823000079

Received: 27 May 2022
Revised: 11 October 2022
Accepted: 1 February 2023
First published online: 22 March 2023

Keywords:
mafic granulites; subduction; slab melting; zircon U–Pb geochronology; Southern Granulite Terrane

Author for correspondence:
JK Tomson,
Email tomson.jk@ncess.gov.in

Abstract

The Precambrian Southern Granulite Terrane (SGT) of south India is well-known for the preservation of high- to ultrahigh-temperature (HT-UHT) granulites, prominently exposed in its central part forming a linear belt referred to as the Kambam UHT belt. This belt also hosts widespread occurrences of mafic granulites that are observed in close spatial association with the HT-UHT granulites. This study presents detailed petrology, geochemistry and geochronology of representative mafic granulites from the area to understand their petrogenesis and tectonic setting. The results demonstrate that mafic granulites are low- to medium-K tholeiites, with continental arc affinity, formed by the partial melting of a subduction-modified enriched mantle source. The composition of the parent mantle source is modelled with a spinel/garnet lherzolite contribution ratio between 100/0 and 70/30, suggesting the mixing of spinel and garnet bearing melts during asthenosphere upwelling. Zircon U–Pb geochronology of mafic granulites constrains their emplacement between 612 Ma and 625 Ma, that subsequently underwent metamorphism between 581 Ma and 531 Ma. This overlaps with the timing of HT-UHT metamorphism in the Kambam UHT belt bracketed between 593 and 532 Ma. Zircon Hf isotopic studies reveal parent magma generation from reworked melting sources involving Archean and Proterozoic components. These results propose an alternative heat source for the formation of HT-UHT granulites in the Kambam UHT belt which can be designated as a major terrane boundary within the SGT.

1. Introduction

Understanding the origin and evolution of mafic rocks and characterizing their source composition can provide crucial insights into the tectonic settings associated with their mode of formation. It is now well-known that in a collisional orogenic environment, mafic rocks are generated either in a subduction-driven post-collisional scenario involving slab break-off, lithospheric delamination and partial melting (Kay & Kay, 1993; Song *et al.*, 2015, among many others) or during continental rifting associated with lithospheric extension (Fairhead, 1988; Wilson, 1989). Collisional orogens are also related to elevated thermal regimes (>900 °C), leading to the formation of high- to ultrahigh-temperature (HT-UHT) metamorphic rocks due to high mantle heat flow before orogenesis (Clark *et al.* 2015 and references therein). As ultra-hot collisional orogens are closely linked to the formation of supercontinents across the globe (Brown, 2007; Kelsey & Hand, 2015), the role of mafic magmatism in the generation of HT-UHT granulites needs to be examined in detail.

The Precambrian Southern Granulite Terrane (SGT; Fig. 1a) of India that occupies a central position in the east Gondwana supercontinent assembly is known for its high geotherm prevalence associated with intense crustal reworking and melting that has also affected other Gondwanan crustal fragments during the Himalayan-scale collision orogen referred to as the East African Orogen (650–480 Ma; Collins *et al.* 2014 and references therein). The SGT has proliferous occurences of HT-UHT metapelites primarily reported in the Madurai block, where these rocks are mostly seen aligned along the transcrustal Suruli shear zone (SSZ), later named as the Kambam UHT belt (KUB; Brandt *et al.* 2011, 2014; Dev *et al.* 2021; Fig. 1a). The heat source responsible for the formation of HT-UHT rocks in the Kambam UHT belt is interpreted to be due to the equilibration at the root of collisional mountain belt with required thermal input for crustal heating by upwelling of hot asthenosphere (Brandt *et al.* 2011, 2014), or due to conductive heating associated with the accumulation of moderately enriched heat-producing elements (HPE) in the crust during collisional orogeny (Clark *et al.* 2015) or due to a combination of tectonic-driven processes including HPE enrichment and equilibration at the continental root (Dev *et al.* 2021). Also, in many Precambrian collisional orogens, mafic magmatism has been proposed as an alternative heat source for regional-scale HT-UHT metamorphism (Kelsey & Hand, 2015 for review). The Kambam UHT belt hosts voluminous mafic

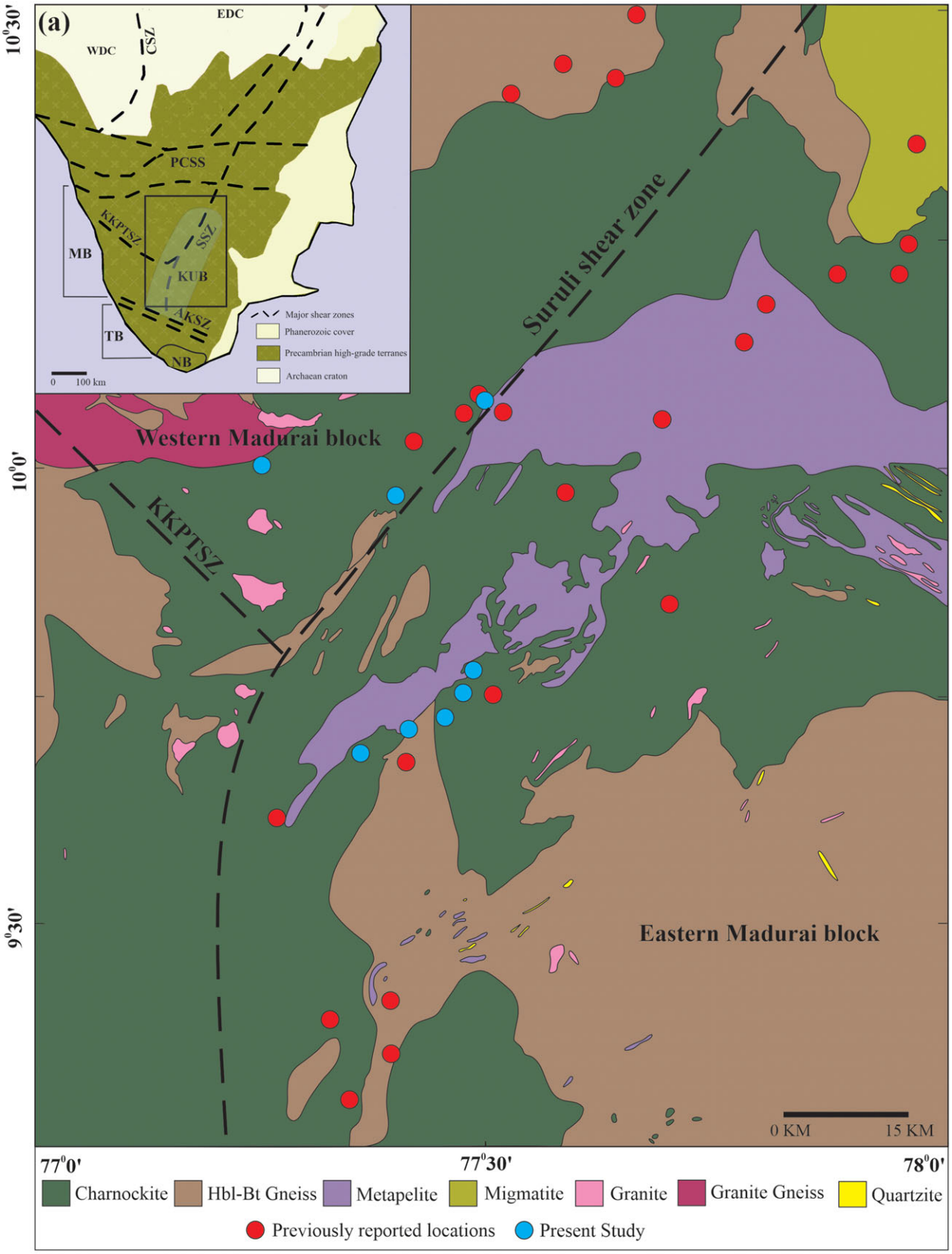

Fig. 1. (Colour online) (a) Simplified geological map of Madurai block (modified after GSI, unpub. map, 1981). Inset shows Southern Granulite Terrane (modified after Kumar *et al.* 2017). Madurai block (MB), Trivandrum block (TB), Nagercoil block (NB), Palghat–Cauvery shear system (PCSS), Suruli shear zone (SSZ), Karur–Kambam–Painavu–Trichur shear zone (KKPTSZ), Achankovil shear zone (AKSZ) and Kambam UHT Belt (KUB).

https://doi.org/10.1017/S0016756823000079 Published online by Cambridge University Press

granulites that are found in close spatial association with HT-UHT granulites. However, tectonic models proposed for this UHT belt have failed to examine whether the mafic emplacements have played any role in generating extreme thermal conditions. In this context, the present study assumes significance, as it aims for a detailed understanding of the petrogenesis of hitherto unreported mafic granulites from the area, and its implications on the current understanding of the tectonic evolution of Kambam UHT belt.

2. Geological setting

Southern Granulite Terrane (SGT) is a composite of polymetamorphic terrains with prolonged crustal evolution history ranging from early Archaean to late Neoproterozoic, preserving the evidence for polyphase deformation, multiple tectonothermal and multiphase exhumation and cooling histories (Ghosh *et al.* 2004; Plavsa *et al.* 2012; Tomson *et al.* 2013; Brandt *et al.* 2014; Collins *et al.* 2014; Kumar *et al.* 2017; Dev *et al.*, 2021; Dev *et al.*, 2022b). SGT is bounded to the north by the Archaean granite–greenstone terrain of the Dharwar craton (Chadwick *et al.* 2000; Jayananda *et al.* 2000). SGT is composed of different crustal blocks named as the Salem, Madurai, Trivandrum and Nagercoil that are separated by crustal-scale shear zones (see Collins *et al.* 2014 for review). The Madurai block, which is the largest crustal block in SGT, constitutes different lithological units such as charnockites, hornblende/garnet biotite gneisses, HT-UHT Mg–Al granulites, quartzites, calc-silicates and two-pyroxene mafic granulites along with intrusives such as syenites, granites, anorthosites and carbonatites. The available structural, geochemical and geochronological data suggest multiple classification schemes for the Madurai block. Ghosh *et al.* (2004) proposed a Neoproterozoic shear zone named the Karur–Kambam–Painavu–Trichur shear zone (KKPTSZ; Fig. 1) within the SGT that defined two distinct terranes within the Madurai block i.e., an Archaean basement terrane to the north and a Proterozoic terrane to the south. The southern limit of KKPTSZ was redesignated as an isotopic boundary by Plavsa *et al.* (2012). Srinivasan and Rajeshdurai (2010) proposed a NE–SW-trending shear zone aligned parallel to the eastern flank of KKPTSZ known as the Suruli shear zone (SSZ; Fig. 1), separating the Madurai block into western and eastern blocks with distinct lithological associations. Brandt *et al.* (2014) designated the area parallel to SSZ as the Kambam ultrahigh-temperature belt (KUB; Fig. 1), owing to the presence of lithological associations characteristic of HT-UHT metamorphism where peak metamorphic conditions up to 1100 °C and 12 kbar with both clockwise and anticlockwise *P–T* trajectories were reported (Dev *et al.* 2021 and references therein).

3. Sampling and petrography

Previous reports on mafic rocks from the Madurai block (red circles in Fig. 1b) are limited to field mapping and thermobarometric studies (Geological Survey of India (GSI), unpub. data; Prakash *et al.* 2007; Ray *et al.* 2021). For the present study, mafic granulite samples were collected from eight newly identified locations along the central part of the Madurai block within the Kambam UHT belt (blue circles in Fig. 1b). Description of the field occurrence and mineralogy of the samples is given in Table 1. The exposures are seen as sub-metre- to metre-scale thick bands, variously associated with quartzites, metapelites and calc-silicate rocks (Fig. 2a–d). The mafic bands are mostly easterly-dipping with a steep slope (Fig. 2a), in conformity with the overall structural trend of the Suruli shear zone (Srinivasan & Rajeshdurai, 2010). No distinct chilled margin is observed in most cases, due to surface weathering. The effect of cooling and deformation in these rocks is evidenced by the presence of joints within these bands (Fig. 2c). At locations where the host metapelites are migmatized, the mafic bands also show similar outcrop features representing large-scale melt movement (Fig. 2d). In addition to thick bands, mafic granulites are also found as boudins and disseminated bands within the host granulites, mainly oriented along the foliation trend but locally forming large shear sense markers (Fig. 2b, d). Petrologically, the rocks are medium-grained with inequigranular granoblastic texture. Major mineral phases include plagioclase, orthopyroxene, clinopyroxene and hornblende with minor amount of quartz, biotite and magnetite (Fig. 3). Accessory phases constitute zircon, rutile and titanite.

4. Analytical methods

4.a. Whole-rock geochemistry

Mafic granulites were crushed into small chips using a jaw crusher and later were fine-powdered using a chrome-steel ring mill at the Thin section and sample preparation laboratory at the National Centre for Earth Science Studies (NCESS), India. The samples were analysed for major elements using a Bruker Pioneer S8 Tiger wavelength-dispersive X-ray fluorescence (WD-XRF) at NCESS following the analytical protocol described in Dev *et al.* (2021). The sample powders were dissolved in a reagent grade HF: HNO_3 acid mixture in Savillex screw-top vessels for trace element and rare earth element (REE) analysis. The analysis was performed using an Agilent 7800 Quadruple ICPMS at the LAM-ICPMS facility, National Geophysical Research Institute, Hyderabad, India. ^{103}Rh was used as the internal standard for sample analysis. G-2, JG-2, GA and AGV-2 were repeatedly analysed to ensure drift correction and calibration. For chondrite normalization, values are chosen from Anders & Grevesse (1989), whereas primitive mantle normalization values are from Sun & McDonough (1989). The whole rock geochemical data was processed and plotted for major and trace element discrimination diagrams using GCDkit 5.0 (Janoušek *et al.* 2006).

4.b. Zircon U–Pb geochronology, trace element and Hf isotope analysis

All samples were crushed and sieved into desirable fractions for conventional Wilfley table-magnetic separation technique. Separated grains were manually handpicked and mounted on a standard epoxy disc of 25 mm diameter. The internal structure of these grains was examined by cathodoluminescence (CL) and back scatter electron (BSE) imaging using CAMECA SXFive-TACTIS electron probe microanalyser (EPMA) at NCESS. Single-spot U–Pb isotope and trace element analysis of zircons was performed at the Isotope Geochemistry Facility (IGF), NCESS, using a Teledyne CETAC, Nd:YAG (solid-state laser) coupled with Agilent 7800 quadrupole ICPMS. The analytical protocol is according (Dev *et al.*, 2022a). 91500 zircon was used as the primary standard, whereas Plesovice and BB11 zircons were monitored for quality check. Data reduction and calculation of isotope ratios and ages were performed offline using Iolite 4.4 (Paton *et al.* 2011) with the integrated Visual Age Package (Petrus & Kamber, 2011), and calculated isotopic ratios and ages were processed using Isoplot 4.15 (Ludwig, 2012). During the analytical session,

https://doi.org/10.1017/S0016756823000079 Published online by Cambridge University Press

Table 1. Field occurrence and major mineral assemblages of mafic granulites

No.	Sample	Field relation	Assemblage
1	KT-MG-18	The sample is exposed in an abandoned roadside quarry. They are found as broken metre-scale bands within the host metapelite. The bands are oriented parallel to the foliation plane of metapelite.	Opx + Cpx + Pl + Hbl +Bt + Rt + Mt + Bt
2	KT-MG-20A	Road cutting exposing large band of mafic granulite co-folded with metapelite, quartzite and calc-silicate. The bands are easterly-dipping and show layer-perpendicular joints.	Opx + Cpx + Pl + Hbl+ Mt + Qtz
3	KT-MG-21	Ground-level exposure exhibiting large easterly-dipping NE–SW-oriented mafic band found in association with metapelite and charnockite.	Opx + Cpx + Pl + Hbl +Kfs + Mt + Qtz
4	KT-MG-24	Ground-level exposure in an abandoned quarry. Large mafic bands are seen with host metapelites. The host metapelites are highly migmatized.	Opx + Cpx + Pl + Hbl +Mt + Qtz + Bt
5	KT-MG-21	Large metre-scale band of mafic granulite within metapelite in an abandoned quarry. The metapelites are highly migmatized and host megaclasts of garnet.	Opx + Cpx + Pl + Hbl +Mt + Qtz
6	KT-MG-27D	Roadside exposure of mafic granulite in association with basement charnockite. The bands are sill-type, and occasionally form decimated large pods within the host rock.	Opx + Cpx + Pl + Hbl +Mt + Qtz
7	KT-MG-29B	Roadside exposure of mafic band found intercalated with metapelite and quartzite. The mafic granulite band is co-folded and fractured.	Opx + Cpx + Pl + Hbl ++ Mt + Qtz
8	KT-MG-32	Road cut exposure of large mafic granulite bands and boudins associated with metapelite and quartzite. The mafic granulites are highly fractured where the host metapelites are highly migmatized.	Opx + Cpx + Pl + Hbl + Mt + Qtz + Bt

Plesovice (Sláma *et al.* 2008) and BB11 (Santos *et al.* 2017) zircons yielded a weighted mean $^{206}Pb/^{238}U$ age of 337 ± 1.5 Ma ($N = 23$) and 560 ± 2.5 Ma ($N = 23$) respectively, all within the reported error limit. For *in situ* trace element determination, NIST 610 (Pearce *et al.* 1997) were used as primary reference standards for time-drift correction and quality monitoring with ^{29}Si (IS value = 14.98 %) as the internal standard. Ti-in-zircon crystallization temperatures (Ferry & Watson, 2007) were calculated using $\alpha_{SiO2} = 1$ and $\alpha_{TiO2} = 0.6$. Hafnium isotopic composition of zircons was analysed at the IGF, NCESS, using a Teledyne CETAC, Nd: YAG (213 nm) solid-state laser coupled with Nu Plasma 3 Multicollector ICPMS (MC-ICPMS). Zircons analysed for U–Pb dating were reanalysed, and spots were positioned close to the previous crater due to spatial limitation. The analytical protocol is according to Dev *et al.* (2021). 91500 zircon and Plesovice zircon were used as the primary standard and quality monitor. Data reduction and calculation of ratios were performed offline using the Hf isotope package in Iolite 4.4 (Paton *et al.* 2011). During the analytical session, Plesovice zircon yielded a standard corrected $^{176}Hf/^{177}Hf$ ratio of 0.282417 ± 0.000029 ($n = 8$) with values within the reported error limit. A ^{176}Lu decay constant of 1.865×10^{-11} yr^{-1} (Scherer *et al.*, 2001) was used to calculate initial Hf isotopic ratios ($^{176}Hf/^{177}Hf$). The initial epsilon Hf and two-stage depleted mantle model ages (T_{DM}) were calculated using chondritic uniform reservoir (CHUR) ratios of $^{176}Hf/^{177}Hf = 0.0332$ and $^{176}Lu/^{177}Hf = 0.282772$ (Blichert-Toft & Albarède, 1997), depleted mantle ratios of $^{176}Hf/^{177}Hf = 0.283251$ (Nowell *et al.* 1998) and $^{176}Lu/^{177}Hf = 0.0384$ (Griffin *et al.* 2000). Calculation of T_{DM} (crustal) ages assumes a $^{176}Lu/^{177}Hf$ ratio of 0.015, corresponding to average continental crust (Griffin *et al.*, 2004). All uncertainties are reported at 2σ confidence level.

5. Geochemistry

Geochemical data of mafic granulites are provided in Appendix 1 in the Supplementary Material available online at https://doi.org/10.1017/S0016756823000079. The samples are characterized by $SiO_2 = 48.74–53.25$ wt %, $Al_2O_3 = 5.74–14.43$ wt %, $TiO_2 = 0.27–2.42$ wt %, $Na_2O = 0.79–2.94$ wt % and $K_2O = 0.22–1.14$ wt %. FeO^T varies between 10.04 and 15.42 wt %, whereas CaO and MgO vary between 8.16 and 13.08 wt % and 4.41 and 20.67 wt %, respectively. Mg# ranges between 0.24 and 0.70. The total alkali ($Na_2O + K_2O$) and K_2O/Na_2O range between 1.46 and 4.06 and 0.18 and 1.13, respectively. In the silica versus total alkali (TAS) diagram (Fig. 4a; Cox *et al.* 1979), the samples fall within the gabbro field and are classified as subalkaline. The tholeiitic nature of the samples is demonstrated in the AFM diagram (Fig. 4b; Irvine & Baragar, 1971), while the $K_2O–SiO_2$ diagram (Fig. 4c; Rollinson, 2014) classifies them as low- to medium-K tholeiites. The samples are characterized by moderate REE enrichment with ∑REE ranging between 48 and 217 ppm and with values 10–100 times to that of chondrite. Chondrite-normalized REE patterns suggests weakly enriched light REE (LREE) ($Sm_N/La_N = 0.36–0.79$) and nearly flat to slightly fractionated heavy REE (HREE) ($Lu_N/Gd_N = 0.46–1.14$) with a prominent negative Eu anomaly (Fig. 5a). The primitive mantle normalized multi-element variation diagram displays the relative enrichment of large-ion lithophile elements (LILE) and weakly negative anomalies of high field strength elements (HFSE), including Nb, Zr and Ti (Fig. 5b).

6. Zircon U–Pb geochronology, and Lu–Hf isotopes and trace element studies

Cathodoluminescence imaging of zircons (Fig. 6) from each sample reveals internal zoning patterns that can be categorized into three types – (1) geometric centres with dark CL, (2) oscillatory zoned cores with dark/bright CL, and (3) planar/sector zoned rims with bright and dark CL that occasionally truncate into inner domains. The zircon U–Pb, trace element and Ti-in-zircon temperature data are presented in Appendix 2, and Hf isotope data of zircons in Appendix 3, in the Supplementary Material available

https://doi.org/10.1017/S0016756823000079 Published online by Cambridge University Press

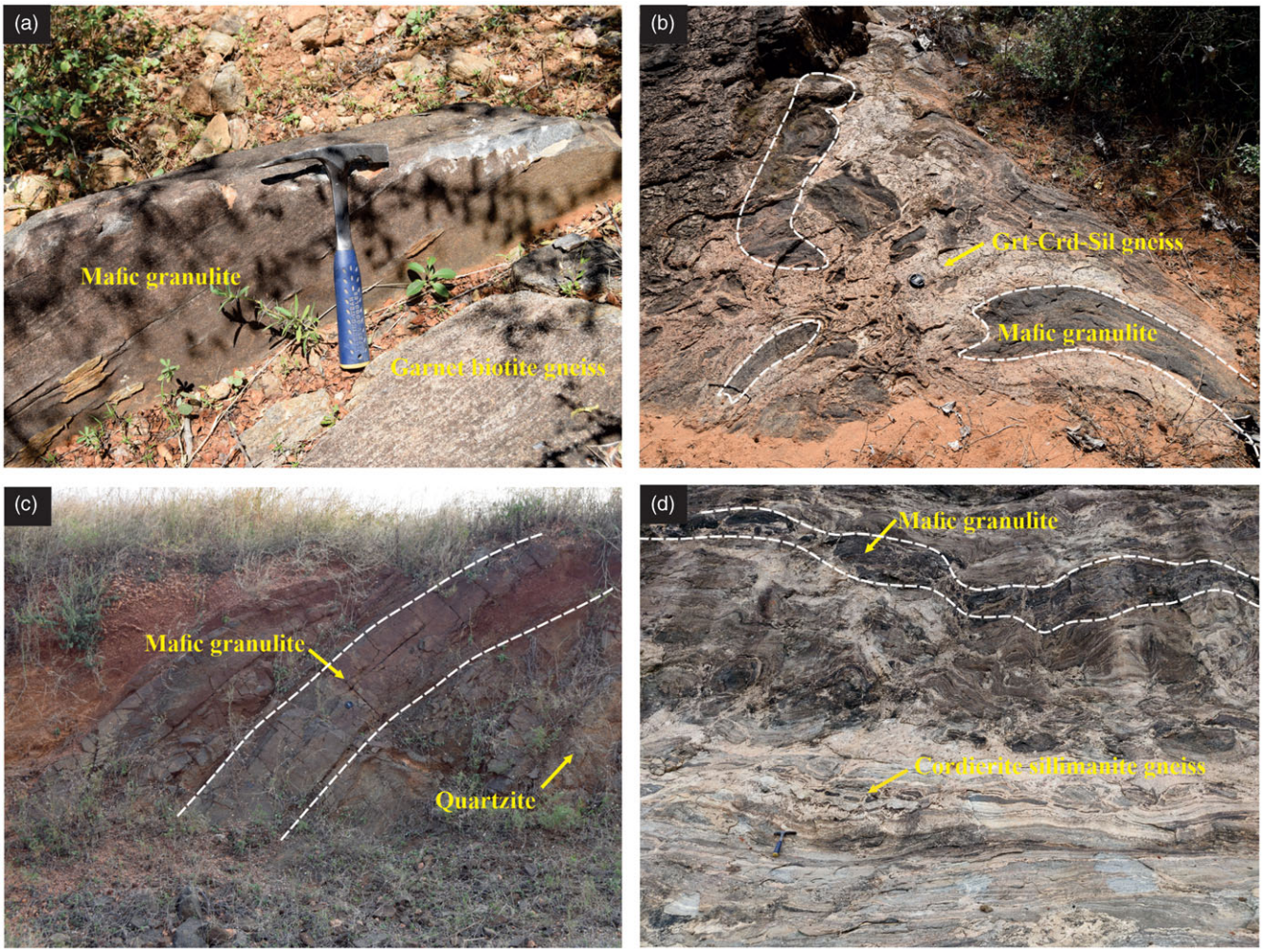

Fig. 2. (Colour online) (a–d): Field photographs of mafic granulites from Kambam UHT Belt: (a) NE–SW-trending mafic granulite band associated with garnet–biotite gneiss; (b) disseminated mafic granulite bands within host metapelite; (c) syn-folded easterly-dipping mafic granulite bands associated with quartzites; and (d) mafic granulite band (occasionally forming boudins) hosted in migmatized metapelites.

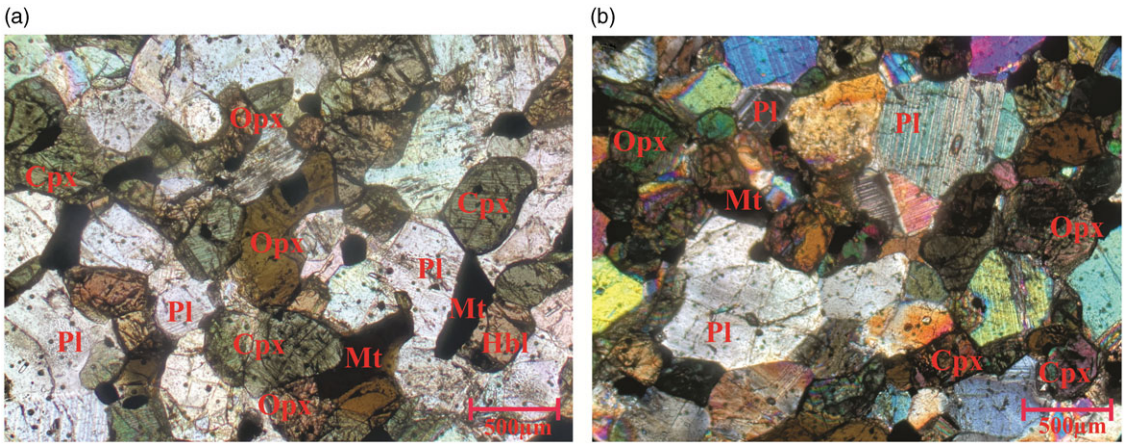

Fig. 3. (Colour online) Representative photomicrographs illustrating mineral assemblages in mafic granulites.

https://doi.org/10.1017/S0016756823000079 Published online by Cambridge University Press

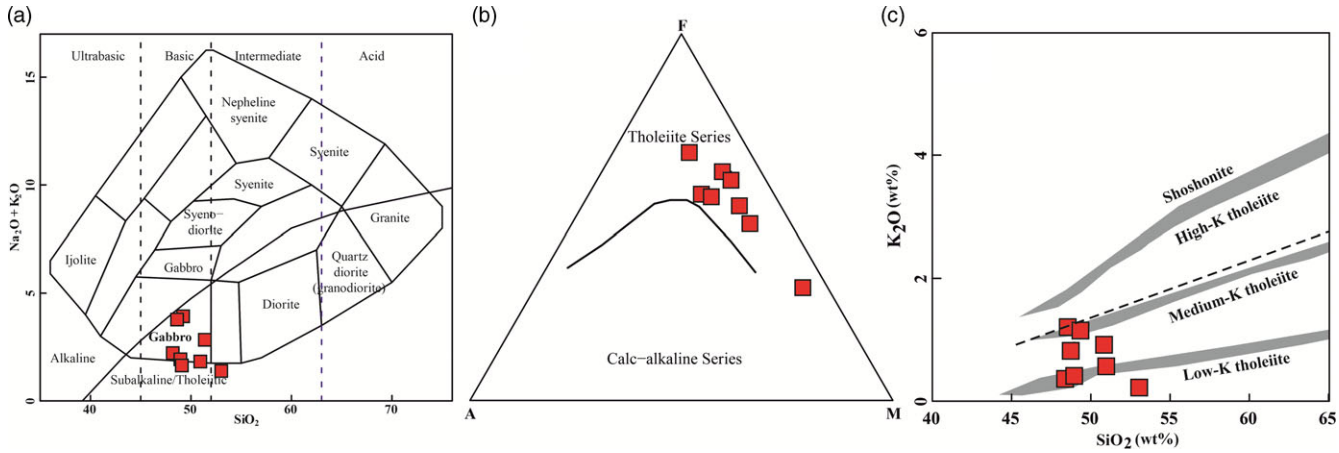

Fig. 4. (Colour online) (a) TAS diagram (after Cox *et al.* 1979); (b) AFM diagram (Irvine & Baragar, 1971); and (c) K_2O–SiO_2 diagram (Rollinson, 2014).

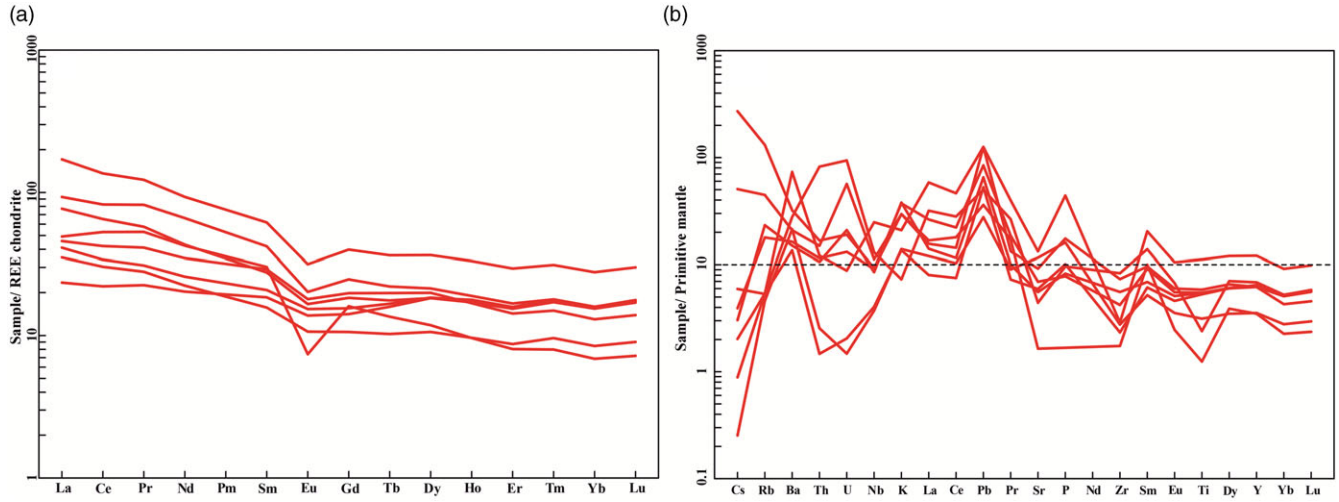

Fig. 5. (Colour online) (a) Chondrite-normalized REE diagram of mafic granulites. (b) Primitive-mantle-normalized trace element diagrams of mafic granulites.

online at https://doi.org/10.1017/S0016756823000079. A summary of U–Pb ages is given in Table 2.

6.a. KT-MG-18

The zircons are characterized by U and Th concentrations of 76–947 ppm and 26–388 ppm, respectively, with Th/U ranging between 0.10 and 1.30. Nineteen U–Pb spot analyses on zircons from the sample yield $^{206}Pb/^{238}U$ age distribution between 522 and 2014 Ma, with a Tera–Wasserburg lower intercept at 545 ± 58 Ma (MSWD = 117) (Fig. 7a). Among these, the oscillatory zoned domains (Th/U = 0.51–1.30) yield a weighted average $^{206}Pb/^{238}U$ age of 619 ± 30 Ma (MSWD = 20) whereas the analyses from planar/sector zoned rims (Th/U = 0.10–0.46) define a weighted average $^{206}Pb/^{238}U$ age of 548 ± 16 Ma (MSWD = 3.8). Chondrite normalized REE pattern of zircons are characterized by positively sloping profile with Lu_N/La_N = 19–1376, Sm_N/La_N = 1–82, Lu_N/Gd_N = 2–25 and Eu/Eu* = 0.03–1.48 (Fig. 8a). Ti concentration in zircons range between 4 and 21 ppm, with Ti-in-zircon temperature estimates varying between 716 and 877 °C (Ferry & Watson, 2007). The Hf isotopic composition of zircons show initial $^{176}Hf/^{177}Hf$ ratios with a narrow range between 0.281760 and 0.281974, whereas $\epsilon_{Hf}(t)$ ranges between −21.08 and −15.6. The calculated Hf–T_{DM} model ages for the sample are between 2.49 and 2.95 Ga.

6.b. KT-MG-20A

Zircons from the sample show U and Th contents of 52–609 ppm and 4–128 ppm respectively, with Th/U ranging between 0.02 and 0.85. U–Pb analyses of 20 spots on zircons yield $^{206}Pb/^{238}U$ age distribution between 546 and 1062 Ma, with a Tera–Wasserburg intercept at 566 ± 37 Ma (MSWD = 11.4) (Fig. 7b). The oscillatory zoned domains of these zircons (Th/U = 0.54–0.85) define a weighted mean $^{206}Pb/^{238}U$ age of 613 ± 40 Ma (MSWD = 10.7), while the rims (Th/U = 0.02–0.49) define a weighted average $^{206}Pb/^{238}U$ age of 573 ± 10 Ma (MSWD = 5.3). Chondrite normalized REE pattern of zircons are characterized by a positively sloping profile with Lu_N/La_N = 13–2778, Sm_N/La_N = 1–90, Lu_N/Gd_N = 2–26 and Eu/Eu* = 0.09–2.28 (Fig. 8b). Ti concentration in zircons ranges between 2 and 18 ppm, with Ti-in-zircon temperature estimates ranging between 645 and 860 °C (Ferry & Watson, 2007). Hf isotopic composition of zircons show initial $^{176}Hf/^{177}Hf$ ratios with a narrow range between 0.282333 and 0.282485. $\epsilon_{Hf}(t)$ ranges between −2.57 and 3.2, and Hf–T_{DM} model ages are between 1.34 and 1.69 Ga.

https://doi.org/10.1017/S0016756823000079 Published online by Cambridge University Press

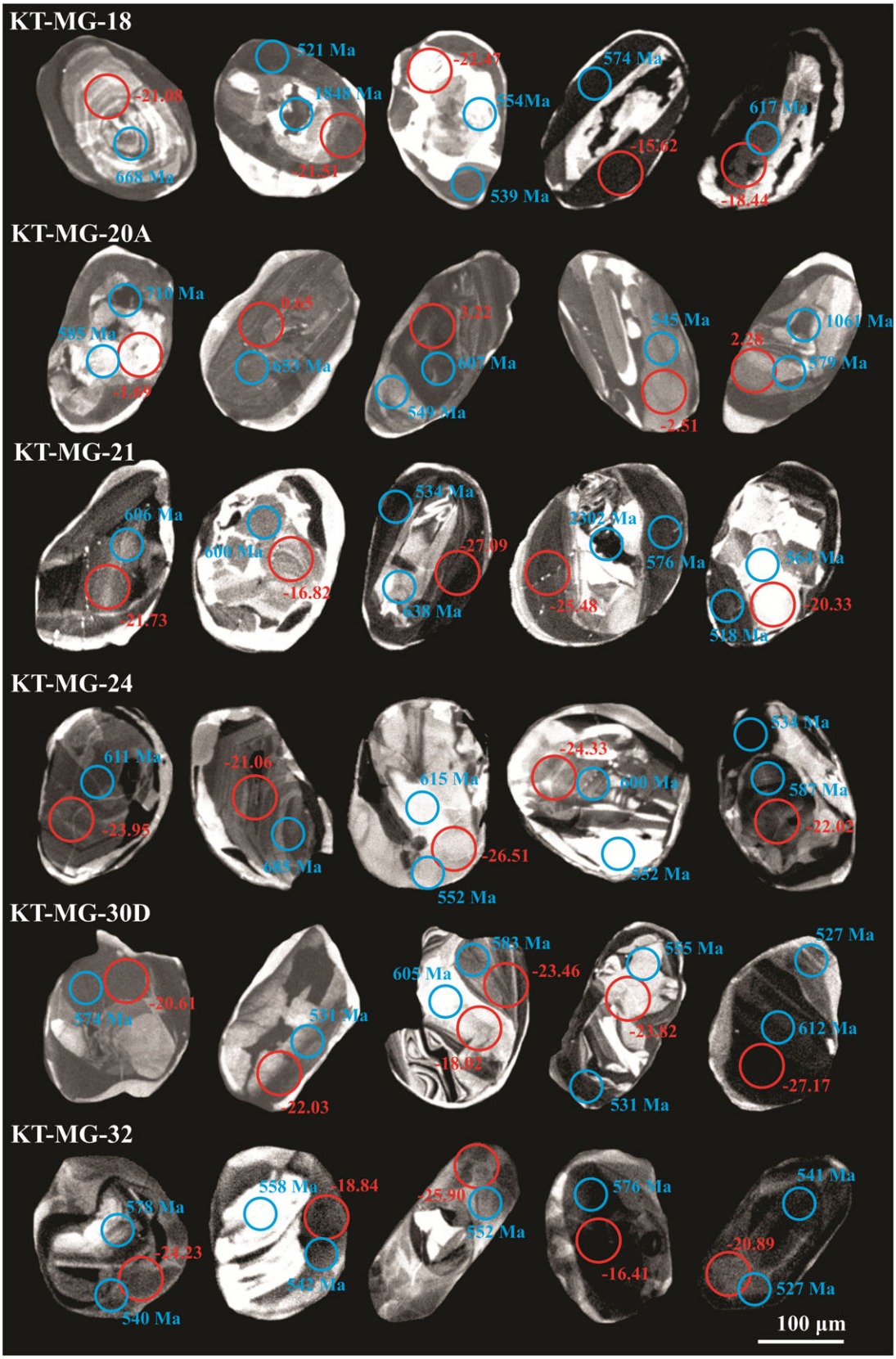

Fig. 6. (Colour online) (a) Cathodoluminescence images of selected zircon grains from mafic granulites. Blue circles mark the position of the laser spot for U–Pb dating and ages are given as $^{206}Pb/^{238}U$ ages (in Ma). Red circles mark the position of Hf isotope analysis with corresponding $\epsilon_{Hf}(t)$ values. Laser spot sizes are scaled to size.

https://doi.org/10.1017/S0016756823000079 Published online by Cambridge University Press

Table 2. Summary of U–Pb data

No.	Sample name	Magmatic age (Ma)	Metamorphic age	
			TW lower intercept age (Ma)	$^{206}Pb/^{238}U$ WM age (Ma)
1	KT-MG-18	619 ± 30	545 ± 58	548 ± 16
2	KT-MG-20A	613 ± 40	566 ± 37	573 ± 10
3	KT-MG-21	625 ± 26	567 ± 30	557 ± 13
4	KT-MG-24	612 ± 25	566 ± 22	570 ± 17
5	KT-MG-30D	619 ± 23	581 ± 33	564 ± 16
6	KT-MG-32	–	531 ± 26	540 ± 10

6.c. KT-MG-21

Twenty-one spot analyses on zircons from the sample yield U concentration between 108 and 733 ppm, Th concentrations between 45 and 856 ppm, and Th/U ratios between 0.10 and 1.26. $^{206}Pb/^{238}U$ ages from the zircons range between 516 and 2302 Ma, with a Tera–Wasserburg lower intercept at 567 ± 30 Ma (MSWD = 14) (Fig. 7c). Among these, the oscillatory zones (Th/U = 0.55–1.26) define a weighted average $^{206}Pb/^{238}U$ age of 625 ± 26 Ma (MSWD = 7.3), whereas the sector/planar zoned rims (Th/U = 0.10–0.46) yield a weighted average $^{206}Pb/^{238}U$ age of 557 ± 13 Ma (MSWD = 8.1). Zircon chondrite normalized REE pattern is characterized by positively sloping profile with Lu_N/La_N = 9–1607, Sm_N/La_N = 1–65, Lu_N/Gd_N = 1–28 and Eu/Eu* = 0.12–1.50 (Fig. 8c). Ti concentration in zircons range between 1 and 20 ppm, yielding Ti-in-zircon temperature estimates between 623 and 939 °C (Ferry & Watson, 2007). The Hf isotopic composition of zircons show initial $^{176}Hf/^{177}Hf$ ratios with a narrow range between 0.281564 and 0.281942, whereas $\epsilon_{Hf}(t)$ ranges between −30.23 and −15.33, and Hf–T_{DM} model ages between 2.51 and 3.37 Ga.

6.d. KT-MG-24

The zircons from the sample have U and Th concentrations of 129–1789 ppm and 44–1742 ppm, respectively. Th/U ratios of zircons vary from 0.09 to 1.74. U–Pb analyses on twenty-one spots define a discordia with a Tera–Wasserburg lower intercept at 566 ± 22 Ma (MSWD = 3.7), and $^{206}Pb/^{238}U$ ages range from 534 to 1654 Ma (Fig. 7d). U–Pb ages from oscillatory zircon domains (Th/U = 0.55–1.74) define a weighted average $^{206}Pb/^{238}U$ age of 612 ± 25 Ma (MSWD = 13), whereas the rims (Th/U = 0.30–0.09) yield a weighted average $^{206}Pb/^{238}U$ age of 570 ± 17 Ma (MSWD = 5.9). Chondrite normalized zircon REE patterns are characterized by positively sloping profile with Lu_N/La_N = 28–13 417, Sm_N/La_N = 2–39, Lu_N/Gd_N = 2–46 and Eu/Eu* = 0.15–1.96 (Fig. 8d). Ti concentration in zircons varies between 4 and 16 ppm, and the estimated Ti-in-zircon temperature values range between 710 and 1021 °C (Ferry & Watson, 2007). The initial $^{176}Hf/^{177}Hf$ ratios of zircons show a narrow range from 0.281680 to 0.281993. $\epsilon Hf(t)$ ranges between −26.51 and −14.93, and Hf–T_{DM} model ages are between 2.44 and 3.13 Ga.

6.e. KT-MG-30D

Nineteen spot analyses on zircons yield U concentrations between 65 and 1196 ppm and Th concentrations between 54 and 427 ppm, yielding Th/U ratios between 0.10 and 1.91. The samples also define a $^{206}Pb/^{238}U$ age spectrum between 510 and 709 Ma, with a Tera–Wasserburg lower intercept at 581 ± 33 Ma (MSWD = 13) (Fig. 7e). Oscillatory domains of zircons (Th/U = 0.58–1.91) define a weighted average $^{206}Pb/^{238}U$ age of 619 ± 23 Ma (MSWD = 13) whereas the rims (Th/U = 0.10–0.37–0.37) yield a weighted average $^{206}Pb/^{238}U$ age of 564 ± 16 Ma (MSWD = 22). Chondrite normalized zircon REE patterns are characterized by a positively sloping profile with Lu_N/La_N = 10–272, Sm_N/La_N = 18–1, Lu_N/Gd_N = 3–17 and Eu/Eu* = 0.75–2.03 (Fig. 8e). Ti concentration in zircons varies between 5 and 16 ppm, yielding Ti-in-zircon temperature estimates between 723 and 847 °C (Ferry & Watson, 2007). The Hf isotopic composition of zircons show initial $^{176}Hf/^{177}Hf$ ratios between 0.281624 and 0.281898. $\epsilon_{Hf}(t)$ ranges from −27.17 to −17.07, and Hf–T_{DM} model ages are between 2.61 and 3.22 Ga.

6.f. KT-MG-32

Zircons from the sample show U and Th concentrations of 565–1316 ppm and 154–673 ppm, yielding Th/U ratios between 0.27 and 0.47. U–Pb analyses on seventeen spots define a discordia with a Tera–Wasserburg lower intercept at 531 ± 26 Ma (MSWD = 1.7), with $^{206}Pb/^{238}U$ age distribution between 510 and 578 Ma (Fig. 7f). U–Pb ages from planar/sector zoned rims (Th/U = 0.27–0.47) zircon domains define a weighted average $^{206}Pb/^{238}U$ age of 540 ± 10 Ma (MSWD = 12). Chondrite normalized zircon REE patterns are characterized by a positively sloping profile with Lu_N/La_N = 297–30 494, Sm_N/La_N = 2–758, Lu_N/Gd_N = 10–31 and Eu/Eu* = 0.08–0.95 (Fig. 8f). Ti concentration in zircons varies from 1 to 15 ppm, with Ti-in-zircon temperature estimates between 611 and 836 °C (Ferry & Watson, 2007). Hf isotopic composition of zircons show initial $^{176}Hf/^{177}Hf$ ratios within the range of 0.281697 and 0.281950, whereas $\epsilon_{Hf}(t)$ ranges between −25.90 and −16.41 and Hf–T_{DM} model age is between 2.53 and 3.10 Ga.

7. Discussion

7.a. Tectonic setting

Whole-rock major and trace element geochemistry of mafic granulites, along with tectonic discrimination diagrams can be used as an effective proxy for identifying their geological settings and the processes responsible for their formation (Cui *et al.* 2021 and references therein). On the TiO_2–MnO–P_2O_5 triangular discrimination diagram (Mullen, 1983), most of the samples fall within the field of continental arc basalts (CAB), validating arc environment for the generation of parent magma (Fig. 9a). The continental arc affinity is further supported by the La/Yb – Nb/La diagram (Hollocher *et al.* 2012), where all samples fall within the continental arc field (Fig. 9b). Geochemical characteristics of these rocks include relative enrichment of LILE and LREE over HFSE with negative anomalies for Nb, Zr and Ti on the primitive mantle normalized multi-element spider diagram (Fig. 5b), all indicative of arc-type magmatism derived from a subduction-modified enriched mantle source (Deevsalar *et al.* 2017; Yang *et al.* 2019 and references therein). Additionally, high La/Nb (1.3–3.1) and La/Ta (9.0–33.3) and low Zr/Ba (0.06–0.59) ratios of the samples are indicative of a subcontinental lithospheric mantle (SCLM) source (Menzies *et al.* 1991; DePaolo & Daley, 2000) whereas high Ba/Ta (97.9–425.8) and Ba/Nb (17.2–56.3) ratios suggest subduction-related magmas (Fitton *et al.* 1988). The enrichment of LILE and LREE with minor fractionation also indicate partial melting and

https://doi.org/10.1017/S0016756823000079 Published online by Cambridge University Press

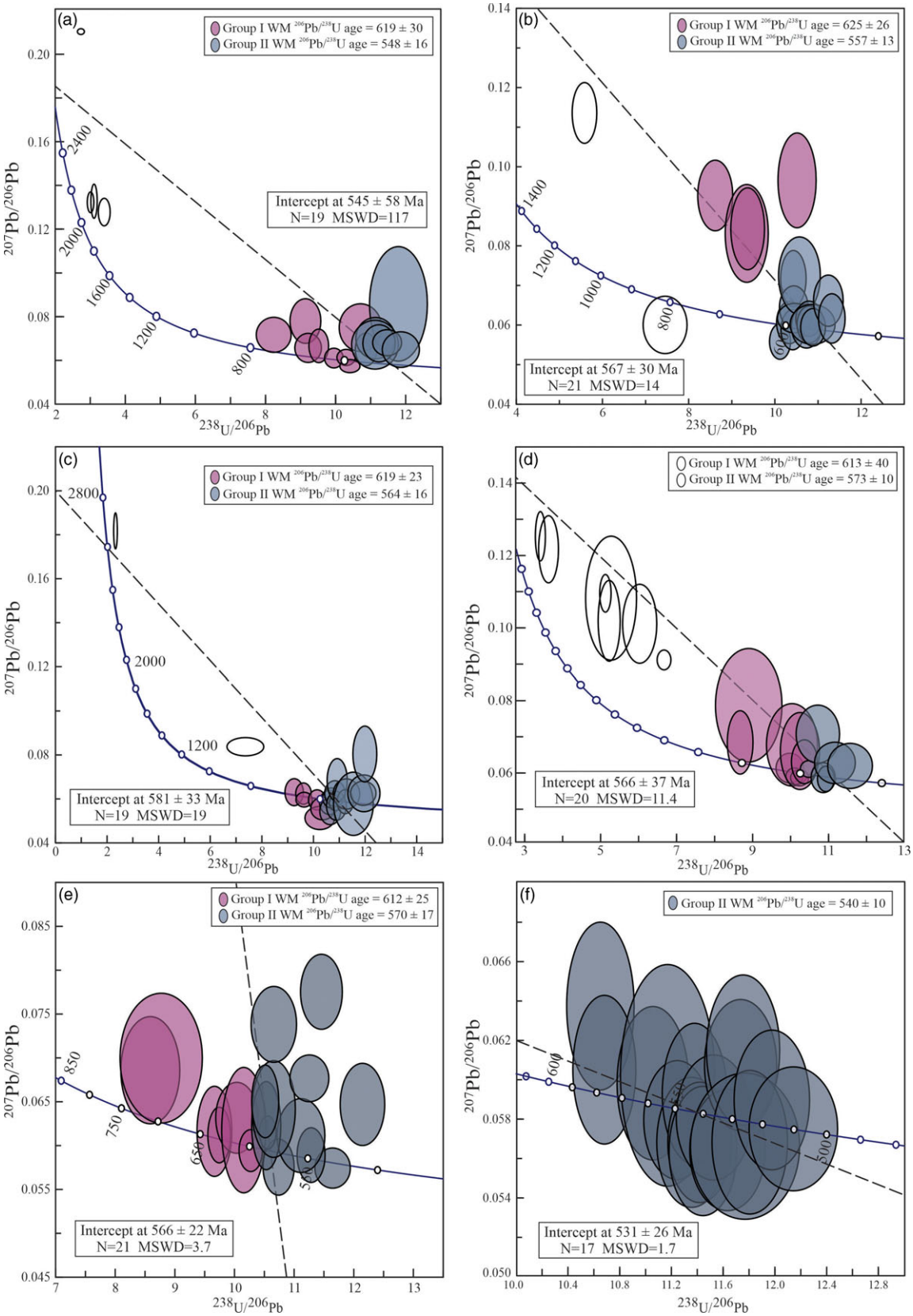

Fig. 7. (Colour online) U–Pb geochronological data of zircons analysed from mafic granulites presented in Tera–Wasserburg diagrams: (a) KT-MG-18; (b) KT-MG-20A; (c) KT-MG-21; (d) KT-MG-24; (e) KT-MG-30D; and (f) KT-MG-32.

https://doi.org/10.1017/S0016756823000079 Published online by Cambridge University Press

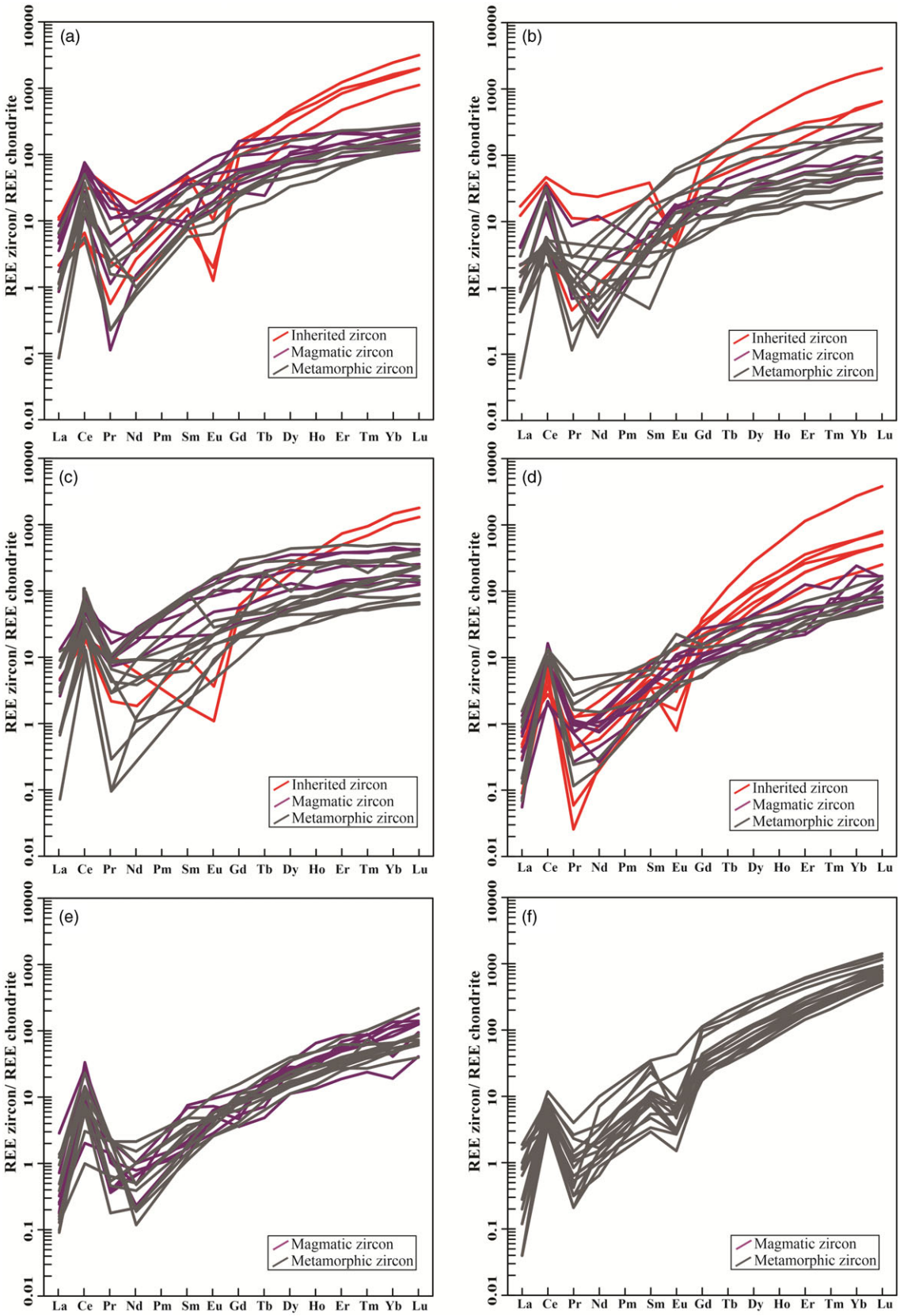

Fig. 8. (Colour online) Chondrite normalized REE pattern of zircons from mafic granulites: (a) KT-MG-18; (b) KT-MG-20A; (c) KT-MG-21; (d) KT-MG-24; (e) KT-MG-30D; and (f) KT-MG-32.

https://doi.org/10.1017/S0016756823000079 Published online by Cambridge University Press

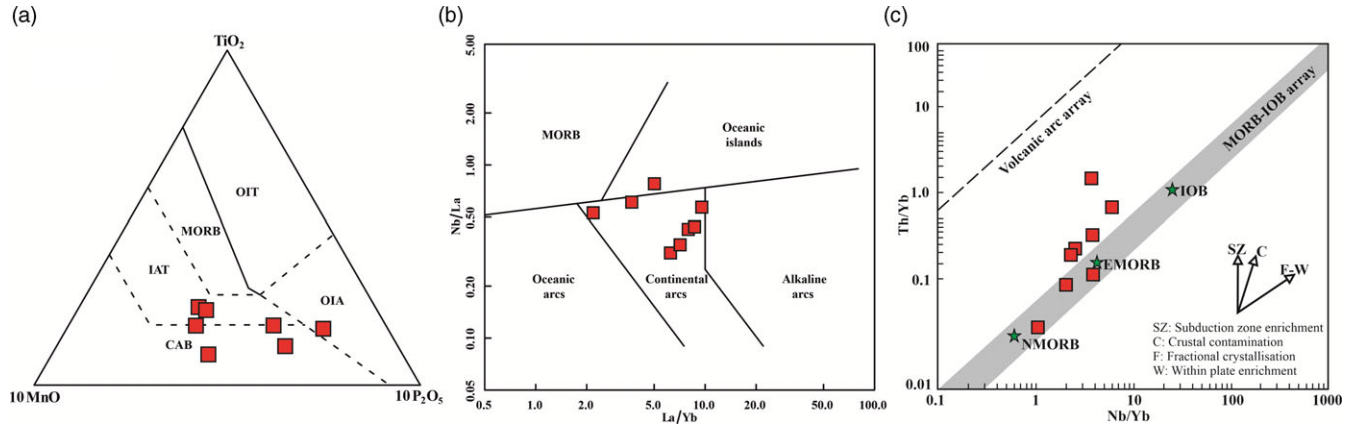

Fig. 9. (Colour online) (a) TiO_2–MnO–P_2O_5 diagram (Mullen, 1983); (b) La/Yb–Nb/La diagram (Hollocher *et al.* 2012); (c) Th/Yb vs Nb/Yb diagram (Pearce, 2008).

metasomatism of the subducted slab (Wang *et al.* 2013), where water-bearing low-density silicate melts from the subducted slab or asthenosphere enriches the source (O'Reilly & Griffin, 2013). The high Sr/Nd (1.8–24.1) ratios and moderately high LILE/HFSE ratios also corroborate the addition of slab-derived fluids, whereas the highly variable Ba/Rb (2.7–150.6) ratios and near-constant low Nb/La (0.32–0.74) ratios also suggest metasomatism in the source region by slab-derived components (Deevsalar *et al.* 2017 and references therein). Moreover, the significant deviation of trace element ratios such as Nb/U (4.7–95.3), Ta/U (0.5–20.4) and Ce/Pb (2.9–14.0) in the sample from mid-ocean ridge basalt (MORB) point to fractionation of these elements in their magma source by non-igneous processes before partial melting of their mantle source, most likely subduction-related (Cui *et al.* 2021). The subduction-assisted mantle source modification is demonstrated by the Th/Yb vs Nb/Yb diagram (Pearce, 2008), where all samples plot above enriched and normal MORB (E- and N-MORB) array (Fig. 9c). The moderately sloping REE patterns ($Lu_N/La_N = 0.15–0.75$) and HREE depletion (Yb < 5) suggest the possible presence of garnet in the melt residue. A mantle source with residual spinel will produce $(Gd/Yb)_N$ ratios of ~1.2 and $(Dy/Yb)_N$ ratio less than 1.5, whereas, for a mantle source with residual garnet, higher $(Gd/Yb)_N$ and $(Dy/Yb)_N$ ratio greater than 2.5 is noted (Deevsalar *et al.* 2017). Additionally, the low $(Gd/Yb)_N$ (0.8–2.3) and $(Dy/Yb)_N$ ratios (1.1–1.7) of the studied samples point to the contribution of spinel and minor garnet in the residual melt. These results suggest the formation of mafic granulites by the melting of a mantle source with garnet and spinel mineralogy, which is either from the garnet–spinel transition zone or by the mixing of garnet and spinel bearing melts. This is more evident from the assimilation and fractional crystallization (AFC) modelling detailed in the following section.

7.b. Crustal contamination and AFC modelling

During emplacement, mantle-derived mafic magmas undergo chemical modification/contamination either due to the assimilation of crustal materials (Khalaf *et al.*, 2011, among many others) or by the thermal erosion of floor rocks (Yang *et al.* 2019 and references therein). In the studied samples, the presence of inherited zircons and strong negative $\epsilon_{Hf}(t)$ values necessitate the examination of the role of crustal contamination in parental magma during emplacement. The wide range of K_2O/P_2O_5 (0.66–6.59) together with TiO_2/P_2O_5 (0.54–7.00) ratios point to the incorporation of silicic crustal components, possibly from a crust of granitic composition (Carlson & Hart, 1988). The ratio between incompatible elements such as Sm/La (0.23–0.49) and TiO_2/Zr (0.01–0.07) of the studied samples are close to the average composition of continental crust (Sm/La = 0.17 and $TiO_2/Zr = 0.003$; Wedepohl, 1995). These values are similar to the basement charnockites reported from the study area (Sm/La = 0.12 and $TiO_2/Zr = 0.002$; Tomson *et al.* 2013), indicating the incorporation of crustal material. The argument for crustal contamination is further discussed using the AFC modelling. For that, we have adopted the La/Sm vs Lu/Yb (Fig. 10) AFC model using the 'PetroGram' Excel spreadsheet of Gündüz and Asan (2021). For melt modelling, non-modal fractional melting was performed with spinel- and garnet lherzolite as end members (Frey, 1980; McDonough, 1990) and primitive-mantle (PM) values (Sun & McDonough, 1989) as the primary melt composition for constructing the AFC line (for input data see Appendix 4 in the Supplementary Material available online at https://doi.org/10.1017/S0016756823000079). The average composition of Madurai block charnockites (Tomson *et al.* 2013) was used for possible contaminant. In the La/Sm vs Lu/Yb diagram, all samples fall along mixing lines between 1 and 2.5 % melts with a spinel/garnet lherzolite contribution ratio between 100/0 and 70/30. Considering PM as the parent source, modelling suggests an AFC up to 66 % (assimilation rate / fractional crystallization rate = 0.29). This indicates the dominance of spinel component in the source, which underwent melting with minor contribution from garnet. This is compatible with the observations from trace element geochemistry pointing to their origin by the mixing of garnet and spinel bearing melts. Similar results are also obtained from the Sm/Yb – Sm plot (Fig. 11; Zhao & Zhou, 2007), suggesting 5–30 % melting of spinel to spinel–garnet lherzolite source. Furthermore, the low Ce/Y ratios for these rocks (<2.5) are suggestive of parent melt generation within the spinel–garnet stability field at a depth of *c.* 60–80 km (McKenzie & Bickle, 1988). As the spinel–garnet transition boundary is expected at a depth of ~80 km (Takahashi & Kushiro, 1983), the lithosphere beneath Madurai block is likely to be dominated by spinel–lherzolite where the incorporation of garnet–lherzolite into these components could have been initiated by the upwelling asthenosphere resulting in the formation of a mixed mantle source for parent melt generation.

7.c. Zircon U–Pb, trace element and Hf isotope data

Zircon U–Pb, trace element and Hf data obtained from LA-ICPMS/LA-MC-ICPMS are discussed following the data presented

https://doi.org/10.1017/S0016756823000079 Published online by Cambridge University Press

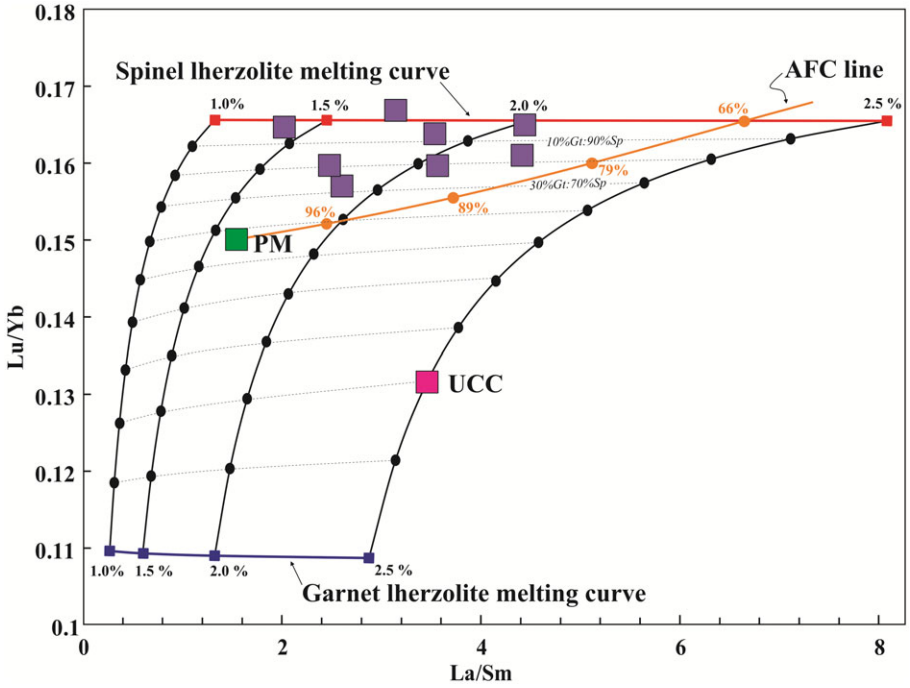

Fig. 10. (Colour online) Assimilation and fractional crystallization (AFC) model using La/Sm vs Lu/Yb bivariant diagram for mafic granulites. UCC: Upper continental crust; PM: primitive mantle.

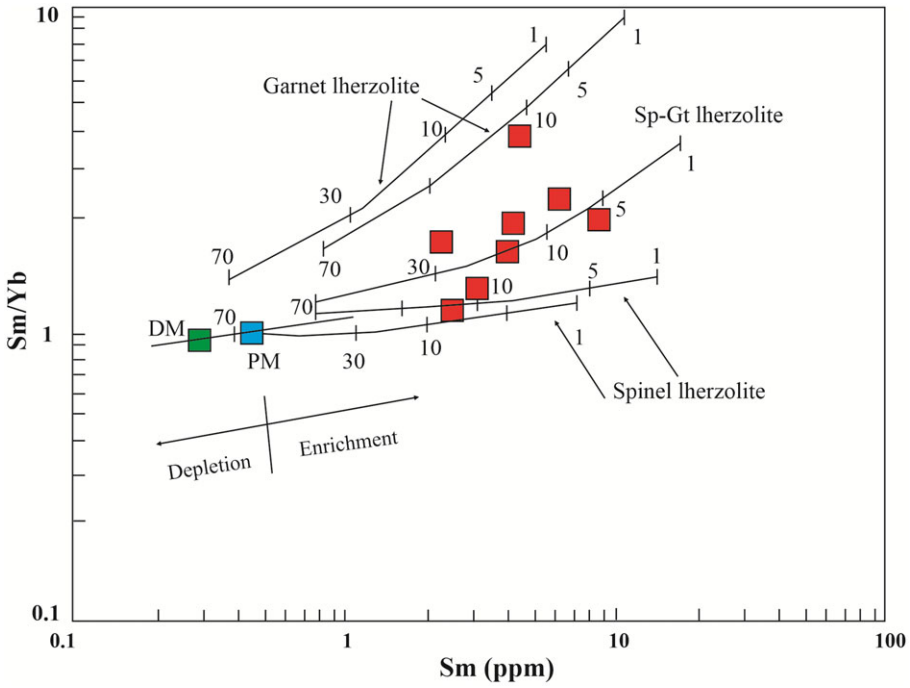

Fig. 11. (Colour online) Sm/Yb – Sm plot (Zhao & Zhou, 2007). DM: depleted mantle, PM: primitive mantle.

in Section 6. In general, the geometric centres of the zircons with dark CL are characterized by higher HREE enrichment and strong negative Eu anomaly compared to the oscillatory zoned and planar/sector zoned domains. These cores produce older (>750 Ma) strongly discordant ages with variable Th/U ratios. Zircons with similar U–Pb ages and chemical characteristics are reported from basement charnockites in the study area by Kumar *et al.* (2017). These basement charnockites are identified as the prominent contributor to the chemical contamination of these rocks, as revealed from AFC modelling (Fig. 10). In addition, the whole-rock geochemistry of the mafic granulites reveals significant depletion in Zr and Hf, indicating retention of minor zircons in the slab residue as inherited magmatic crystals (Rubatto & Hermann, 2003). Hence the older ages obtained from the samples are interpreted as inherited ages. U–Pb ages obtained from oscillatory zones within zircons and their high Th/U ratio (>0.5) suggest their formation by magmatic crystallization. The weighted mean $^{206}Pb/^{238}U$ ages from these domains range from 612 ± 25 Ma to 625 ± 26 Ma, which is interpreted as the timing of mafic magmatism in the area (Table 2). The high MSWD associated with these ages can be due to partial Pb loss during subsequent high-grade metamorphism (Takamura *et al.* 2020) and is reported from the terrane by many workers (Brandt *et al.*, 2014; Dev *et al.*, 2022a). The planar/sector zoned rim domains

https://doi.org/10.1017/S0016756823000079 Published online by Cambridge University Press

show distinct low Th/U ratios (<0.5), and ages from this group represents the timing of metamorphism recorded in the mafic granulites bracketed between 573 ± 10 Ma and 540 ± 10 Ma. These ages are also in agreement with the timing of HT-UHT metamorphism reported from SGT, which suggests the prevalence of a long-lived HT metamorphic event in the area, spanning at least ~35 Ma. This is similar to earlier studies that proposed ~40 Ma duration for the HT-UHT metamorphism in Madurai block (Clark *et al.*, 2015; Dev *et al.*, 2021).

Trace element analyses of the zircons from the mafic granulites demonstrate arc affinity by their high U/Yb (>1) ratio. In contrast, the negative correlations between Ti and Hf concentrations reveal imprints of a fractional crystallization process associated with parent magma generation (Kohn *et al.* 2017 and references therein). The considerably high Hf and low Zr/Hf ratio in these zircons also indicate their growth from a fractionated melt (Fu *et al.*, 2008). In the Y vs U/Yb zircon discrimination diagram (Grimes *et al.* 2007), most of the samples fall within the continental zircon field, supporting the proposed continental arc origin for the samples (Fig. 12a). The Lu_N/Gd_N vs U–Pb age plot (Fig. 12b) indicate that, younger zircons have higher Lu_N/Gd_N values than older ones. An increase in Lu_N/Gd_N values suggest the breakdown of minerals enriched in HREE, possibly garnet that supplied HREEs during the zircon growth (Rubatto *et al.* 2013). Since the studied samples are garnet absent, the HREE enrichment in zircons can be either sourced from the breakdown of garnet in the parent melt or from the garnet bearing basement charnockites that are identified as the significant contaminant source of these rocks.

Hafnium isotope data of zircons show two tight population groups: (1) samples with $^{176}Hf/^{177}Hf$ ranging between 0.281564 and 0.281993 and $\epsilon_{Hf}(t)$ values ranging between −30.23 and −14.93, and (2) samples with higher $^{176}Hf/^{177}Hf$ between 0.282333 and 0.282485 and $\epsilon_{Hf}(t)$ values between −2.57 and 3.22 (Fig. 13a). The former samples have T_{DM} ages between 2.44 Ga and 3.37 Ga, whereas the latter group includes T_{DM} ages between 1.34 Ga and 1.69 Ga. This points to the involvement of two distinct parental sources in magma generation (Fig. 13a). The samples with older T_{DM} ages and highly negative $\epsilon_{Hf}(t)$ values suggest extreme reworking of a Archean to Palaeoproterozoic melting source. In contrast, the younger T_{DM} ages and near-positive $\epsilon_{Hf}(t)$ values point to a considerably lower degree of reworking of a Mesoproterozoic source with juvenile signatures for the generation of parental magma. However, all these samples were emplaced during the late Neoproterozoic, evidenced by their similar magmatic ages between 612 and 625 Ma obtained from oscillatory zoned domains. This is also shown in the T_{DM} age vs U–Pb age diagram (Fig. 13b), where a mixing trend is observed at this magmatic age window, suggesting the mixing of different sources. Pb loss characterizes the post emplacement period, observed around ~580 Ma (from Fig. 13b), which also overlaps with the oldest metamorphic age recorded in the samples (KT-MG-30D: 581 ± 33 Ma), resulting from the widespread Neoproterozoic metamorphism that affected the terrane.

7.d. Geodynamic implications

As discussed in the foregoing, the Ediacaran–Cambrian Gondwana assembly was associated with the development of UHT metamorphic assemblages in the Kambam UHT belt, with heat supplied either by HPE enrichment or equilibration at the continental root or by a combination of both (Brandt *et al.* 2011; Clark *et al.* 2015; Dev *et al.* 2021). Even though regional-scale HT-UHT granulite formation is commonly linked to any of these processes across the globe (see Kelsey & Hand, 2015 for review), the presence of voluminous, syn-metamorphic mafic or ultramafic emplacements is also considered as an alternative heat source for UHT granulite formation (Kemp *et al.* 2007; Giustina *et al.* 2011; Guo *et al.*, 2012; Klaver *et al.* 2016; Wang *et al.* 2020). In the Kambam UHT belt, UHT metamorphism (593 Ma and 530 Ma) closely follows the emplacement of mafic granulites (612 Ma to 625 Ma) in the area, and the similarity in these ages suggest that advective heating during mafic magmatism combined with asthenospheric upwelling could have triggered UHT metamorphism. Hence, the crust was pre-conditioned by the regional-scale mafic magmatism through which, heat source for UHT metamorphism was sustained for a longer period. Such a pre-conditioning process may not be temporally related to UHT events, i.e. they occur prior to the event or it occurs during a sufficiently long-lived slab window-related event (Kelsey & Hand, 2015 and references therein). This model of an external heat source for UHT metamorphism is in agreement with the results from the adjacent Trivandrum block, where granulite formation exclusively by HPE enrichment is considered implausible without thermal input from an external source (Nandakumar & Harley, 2019). In addition to these mafic granulites, closely associated voluminous igneous rocks (charnockites, granites and syenites) with coeval emplacement ages (our unpublished data) can also contribute heat to sustain such a long-lived UHT orogen.

Geochemical and geochronological studies constrain a subduction–collisional tectonic environment for the emplacement and metamorphism of these mafic granulites. Hafnium isotopic signatures suggest parental magma generation from both Archean and Proterozoic melting sources with different degrees of reworking. The calculated T_{DM} model ages and $\epsilon_{Hf}(t)$ values for these rocks are in good agreement with the reported values of associated rocks from the study area (Kumar *et al.* 2017). The remarkable agreement of T_{DM} model ages with the whole-rock Sm–Nd model ages of rocks from this domain (Plavsa *et al.* 2012; Tomson *et al.* 2013) indicates the involvement of Archean and Proterozoic melting sources. Similar meta-gabbros/mafic granulites have been reported from other Gondwanan counterparts such as Trivandrum block (Yang *et al.* 2019), Nagercoil block (Sajna *et al.* 2022; Kroner *et al.* 2015), Sri Lanka (Santosh *et al.* 2014; Takamura *et al.* 2015) and Antarctica (Takamura *et al.* 2020), with similar emplacement/metamorphic ages suggesting that this Neoproterozoic mafic magmatism is a pervasive igneous event that can be traced across different East Gondwana fragments. Together with previously published results, these inferences suggest a collision setting between western Madurai block and eastern Madurai block along the Kambam UHT belt and Suruli shear zone. This observation is in agreement with previous studies interpreting the Kambam UHT belt and Suruli shear zone as a Neoproterozoic collisional boundary within SGT (Srinivasan & Rajeshdurai, 2010; Brandt *et al.* 2014). This argument is further validated by the contrast in elastic thickness (T*e*) between the western Madurai block and eastern Madurai blocks where the latter has the higher T*e* (Ratheesh-Kumar *et al.* 2020). The location of SSZ also overlaps with the earlier proposed structural arc along the eastern part representing a collisional boundary between western and eastern blocks (Cenki & Kriegsman, 2005).

As SGT and Madurai block forms an integral component in the East Gondwana amalgamation, the significance of the Kambam UHT belt and Suruli shear zone needs to be explored in a terrain boundary perspective and demonstrated using a new tectonic

https://doi.org/10.1017/S0016756823000079 Published online by Cambridge University Press

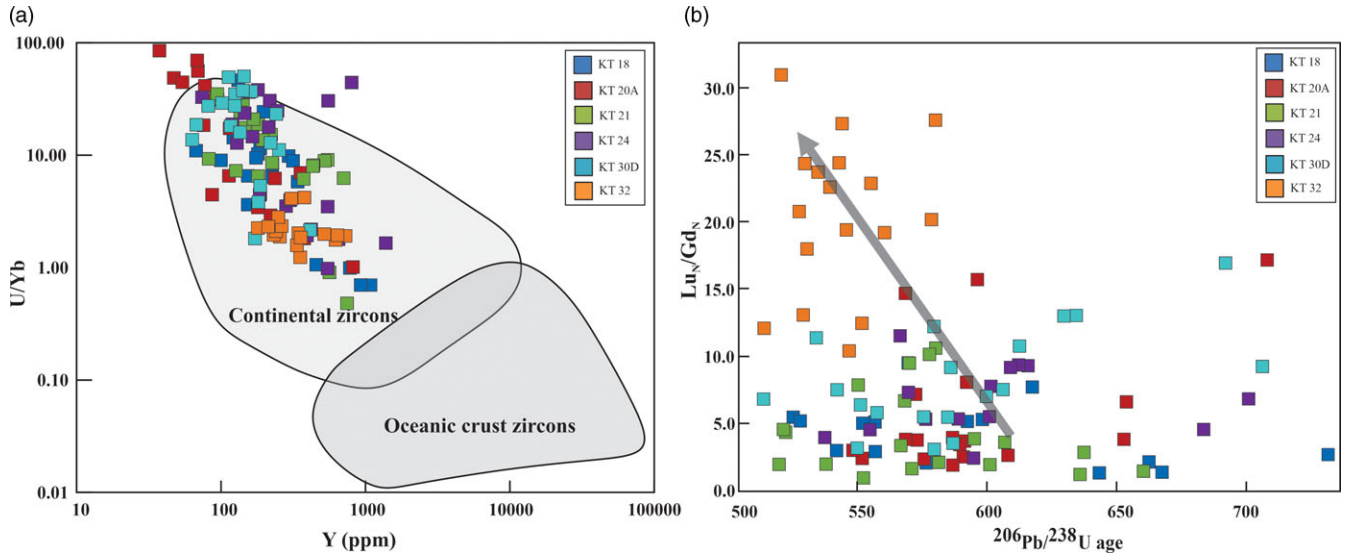

Fig. 12. (a) Y vs U/Yb zircon discrimination diagram (Grimes *et al.* 2007); and (b) Lu_N/Gd_N vs U–Pb age plot for zircons from mafic granulites.

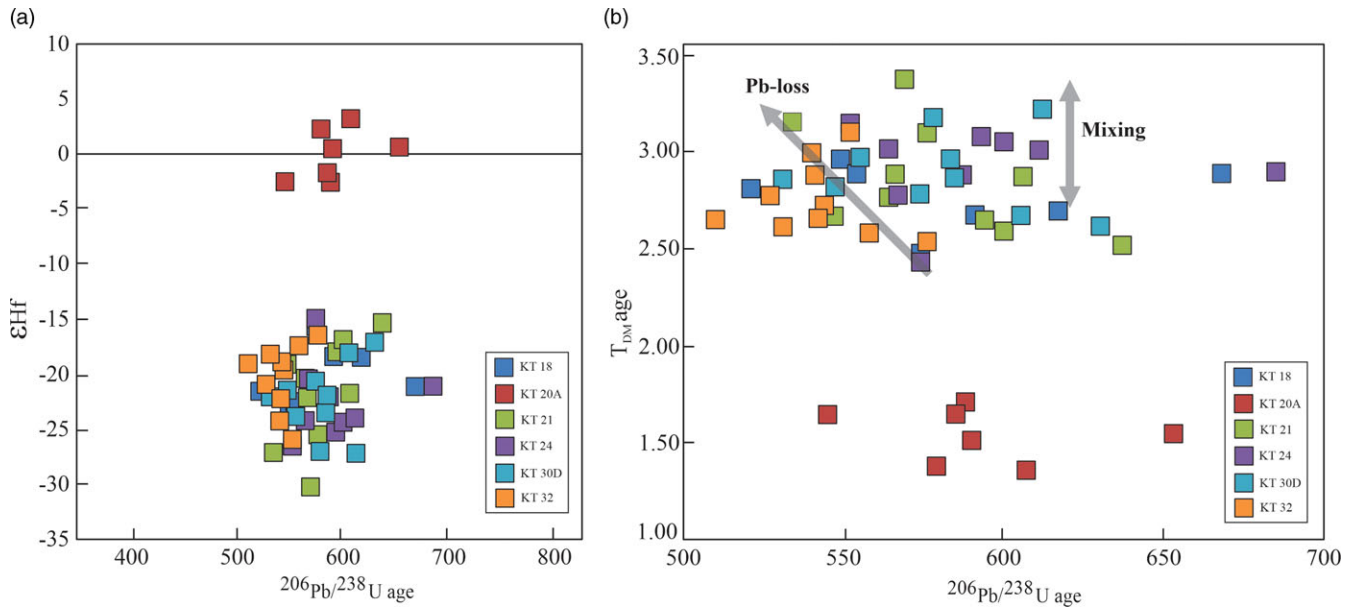

Fig. 13. (a) Age vs $\epsilon_{Hf}(t)$ of zircons; (b) T_{DM} age vs U–Pb age diagram. Mixing and Pb-loss trends are from Zeh *et al.* (2008).

model as illustrated in Fig. 14. Although the exact age of collision between the eastern and western Madurai blocks is unknown, the late Neoproterozoic collision along SSZ resulted in the subduction of SCLM below the eastern Madurai block. Collision led to NW-directed thrusting of the eastern Madurai block onto the western Madurai block (Srinivasan & Rajeshdurai, 2010), initiating significant crustal thickening. The post-collisional extension and slab break following the subduction of SCLM triggered the upwelling of hot asthenosphere, which interacted with the subducted slab and lithospheric basement, forming lower crustal emplacement of these mafic granulites between 612 and 625 Ma. Also, this collisional belt must have acted as a depositional basin for sedimentary units (Collins *et al.* 2014). These sedimentry units were later transformed to HT-UHT metapelites due to advective heating during mafic magmatism along with asthenospheric upwelling and continued orogenic crustal thickening. This proposal of collisional tectonics for UHT metamorphism in Madurai block is validated by the clockwise *P–T* evolution trend (Dev *et al.* 2021 and references therein) which is commonly reported for UHT granulites from collisional orogens across the globe (Brown, 2006, 2007). A continued collision during the Neoproterozoic period resulted in regional-scale deformation and dextral shearing along the Suruli shear zone, and the exhumation of these mafic granulites, which were later co-folded with metapelites and quartzites, forming large-scale interference folding patterns (Srinivasan & Rajeshdurai, 2010). This period is also marked by the emplacement of syn-and post-collisional granitoids along this belt, with coeval emplacement ages (our unpublished data), which might have acted as stitching plutons marking the final phase of the collision. All these evidences argue that the Kambam UHT belt and Suruli shear zone represents

https://doi.org/10.1017/S0016756823000079 Published online by Cambridge University Press

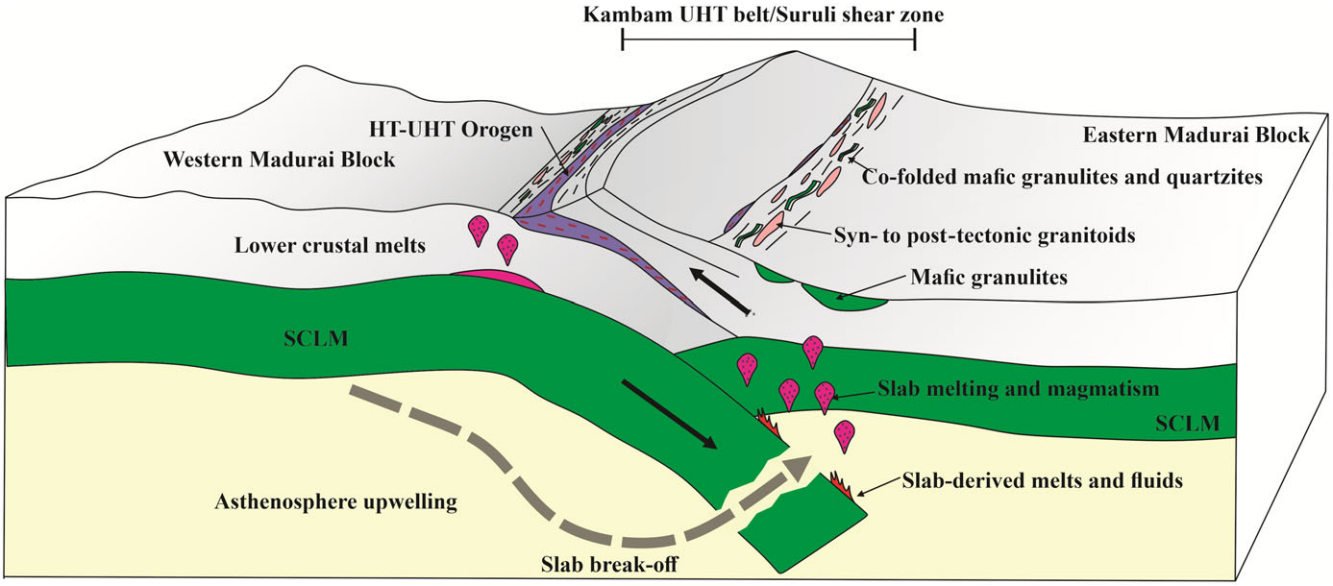

Fig. 14. (Colour online) Schematic illustration of petrogenetic/tectonic model proposed for the generation of mafic granulites and associated lithologies in KUB.

a Neoproterozoic collisional boundary in the Madurai block within the SGT, associated with the final stage of Gondwana supercontinent assembly.

8. Conclusion

Geochemical, geochronological and isotopic studies of mafic granulites within the Kambam UHT belt located along the Suruli shear zone in the Madurai block of SGT throws light on their petrogenesis and tectonic setting. Geochemistry of the samples reveals their low- to medium-K tholeiitic nature with arc affinity. The mafic granulites are formed by the partial melting of a subduction-modified enriched mantle source that has been modelled with a spinel/garnet lherzolite contribution ratio between 100/0 and 70/30. Zircon U–Pb geochronology of the samples constrains their emplacement age between 612 Ma and 625 Ma and metamorphism between 581 Ma and 531 Ma. This overlaps with the timing of HT-UHT metamorphism in the Kambam UHT belt, offering an alternative view on the heat source responsible for the formation of HT-UHT granulites. Zircon Hf isotopic studies of the samples reveal the involvement of reworked mixed melting source in the generation of parental magma. In light of the above, a collisional tectonic model is proposed to explain the formation of mafic granulites involving the western and eastern Madurai blocks along the Kambam UHT belt and Suruli shear zone.

Supplementary material. To view supplementary material for this article, please visit https://doi.org/10.1017/S0016756823000079

Acknowledgements. The authors thank Director, NCESS for providing unconditional support to carry out this work. Dr Sneha Mukherjee, Mr K Eldhose, Mr N Nishanth and Mr Sarath Kumar S are acknowledged for support during fieldwork, sample preparation and analysis. ADJ gratefully acknowledges PhD research funding support through the DST-INSPIRE Programme (DST/INSPIRE Fellowship/IF170781). TVK acknowledges the financial support from an in-house project MLP-6406-28(EVB) and thanks Director, CSIR-NGRI for his continuous support and encouragement.

References

Anders E and Grevesse N (1989) Abundances of the elements: meteoritic and solar. *Geochimica et Cosmochimica Acta* **53**, 197–214.

Blichert-Toft J and Albarède F (1997) The Lu-Hf isotope geochemistry of chondrites and the evolution of the mantle-crust system. *Earth and Planetary Science Letters* **148**, 243–58.

Brandt S, Raith MM, Schenk V, Sengupta P, Srikantappa C and Gerdes A (2014) Crustal evolution of the Southern Granulite Terrane, south India: new geochronological and geochemical data for felsic orthogneisses and granites. *Precambrian Research* **246**, 91–122.

Brandt S, Schenk V, Raith MM, Appel P, Gerdes A and Srikantappa C (2011) Late Neoproterozoic PT evolution of HP-UHT granulites from the Palni Hills (South India): new constraints from phase diagram modelling, LA-ICP-MS zircon dating and in-situ EMP monazite dating. *Journal of Petrology* **52**, 1813–56.

Brown M (2006) Duality of thermal regimes is the distinctive characteristic of plate tectonics since the Neoarchean. *Geology* **34**, 961–4.

Brown M (2007) Metamorphic conditions in orogenic belts: a record of secular change. *International Geology Review* **49**, 193–234.

Carlson RW and Hart WK (1988) Flood basalt volcanism in the northwestern United States. In *Continental Flood Basalts* (ed. JD Macdougall), pp. 35–61. Dordrecht: Springer.

Cenki B and Kriegsman LM (2005) Tectonics of the Neoproterozoic southern granulite terrain, South India. *Precambrian Research* **138**, 37–56.

Chadwick B, Vasudev VN and Hegde GV (2000) The Dharwar craton, southern India, interpreted as the result of Late Archaean oblique convergence. *Precambrian Research* **99**, 91–111.

Clark C, Healy D, Johnson T, Collins AS, Taylor RJ, Santosh M and Timms NE (2015) Hot orogens and supercontinent amalgamation: a Gondwanan example from southern India. *Gondwana Research* **28**, 1310–28.

Collins AS, Clark C and Plavsa D (2014) Peninsular India in Gondwana: the tectonothermal evolution of the Southern Granulite Terrain and its Gondwanan counterparts. *Gondwana Research* **25**, 190–203.

Cox KG, Bell JD and Pankhurst RJ (1979) *The Interpretation of Igneous Rocks*. London: George, Allen and Unwin, 450 pp.

Cui X, Sun M, Zhao G and Zhang Y (2021) Origin of Permian mafic intrusions in southern Chinese Altai, Central Asian Orogenic Belt: a post-collisional extension system triggered by slab break-off. *Lithos* **390**, 106112.

Deevsalar R, Shinjo R, Ghaderi M, Murata M, Hoskin PWO, Oshiro S, Wang KL, Lee HY and Neill I (2017) Mesozoic–Cenozoic mafic magmatism in Sanandaj–Sirjan zone, Zagros Orogen (Western Iran): geochemical and isotopic inferences from middle Jurassic and late Eocene gabbros. *Lithos* **284**, 588–607.

DePaolo DJ and Daley EE (2000) Neodymium isotopes in basalts of the southwest basin and range and lithospheric thinning during continental extension. *Chemical Geology* **169**, 157–85.

Dev JA, Tomson JK, Sorcar N and Francis KA (2022a) Timing of UHT metamorphism and cooling in south Indian granulites: New PTt results from a sapphirine granulite. *Precambrian Research*, **371**, 106582.

Dev JA, Sorcar N, Mukherjee S and Tomson JK (2022b) Phase equilibrium modelling and zircon-monazite geochronology of HT-UHT granulites from Kambam ultrahigh-temperature belt, south India. *International Geology Review*, 1–19.

Dev JA, Tomson JK, Sorcar N and Nandakumar V (2021) Combined U-Pb/Hf isotopic studies and phase equilibrium modelling of HT-UHT metapelites from Kambam ultrahigh-temperature belt, south India: constraints on tectonothermal history of the terrane. *Lithos*, **406**, 106531.

Fairhead JD (1988) Mesozoic plate tectonic reconstructions of the central South Atlantic Ocean: the role of the West and Central African rift system. *Tectonophysics* **155**, 181–91.

Ferry JM and Watson EB (2007) New thermodynamic models and revised calibrations for the Ti-in-zircon and Zr-in-rutile thermometers. *Contributions to Mineralogy and Petrology* **154**, 429–37.

Fitton JG, James D, Kempton PD, Ormerod DS and Leeman WP (1988) The role of lithospheric mantle in the generation of late Cenozoic basic magmas in the western United States. *Journal of Petrology*25, 331–49.

Frey FA (1980) The origin of pyroxenites and garnet pyroxenites from Salt Lake Crater, Oahu, Hawaii: trace element evidence. *American Journal of Science*, **280**, 427–49.

Fu B, Page FZ, Cavosie AJ, Fournelle J, Kita NT, Lackey JS, Wilde S and Valley JW (2008) Ti-in-zircon thermometry: applications and limitations. *Contributions to Mineralogy and Petrology* **156**, 197–215.

Ghosh JG, de Wit MJ and Zartman RE (2004) Age and tectonic evolution of Neoproterozoic ductile shear zones in the Southern Granulite Terrain of India, with implications for Gondwana studies. *Tectonics* **23**, TC3006.

Giustina MESD, Pimentel MM, Ferreira Filho CF and de Hollanda MHBM (2011) Dating coeval mafic magmatism and ultrahigh temperature metamorphism in the Anápolis-Itauçu Complex, Central Brazil. *Lithos* **124**, 82–102.

Griffin WL, Belousova EA, Shee SR, Pearson NJ and O'Reilly SY (2004) Archean crustal evolution in the northern Yilgarn craton: U-Pb and Hf-Isotope evidence from detrital zircons: *Precambrian Research*, **131**, 231–82.

Griffin WL, Pearson NJ, Belousova E, Jackson SV, Van Achterbergh E, O'Reilly SY and Shee SR (2000) The Hf isotope composition of cratonic mantle: LAM-MC-ICPMS analysis of zircon megacrysts in kimberlites. *Geochimica et Cosmochimica Acta* **64**, 133–47.

Grimes CB, John BE, Kelemen PB, Mazdab FK, Wooden JL, Cheadle MJ, Hanghøj K and Schwartz JJ (2007) Trace element chemistry of zircons from oceanic crust: a method for distinguishing detrital zircon provenance. *Geology* **35**, 643–6.

Gündüz M and Asan K (2021) PetroGram: an Excel-based petrology program for modeling of magmatic processes. *Geoscience Frontiers* **12**, 81–92.

Guo J, Peng P, Chen Y, Jiao S and Windley BF (2012) UHT sapphirine granulite metamorphism at 1.93–1.92 Ga caused by gabbronorite intrusions: implications for tectonic evolution of the northern margin of the North China Craton. *Precambrian Research* **222**, 124–42.

Hollocher K, Robinson P, Walsh E and Roberts D (2012) Geochemistry of amphibolite-facies volcanics and gabbros of the Støren Nappe in extensions west and southwest of Trondheim, Western Gneiss Region, Norway: a key to correlations and paleotectonic settings. *American Journal of Science* **312**, 357–416.

Irvine TN and Baragar WRA (1971) A guide to the chemical classification of the common volcanic rocks. *Canadian Journal of Earth Sciences* **8**, 523–48.

Janoušek V, Farrow CM and Erban V (2006) Interpretation of whole-rock geochemical data in igneous geochemistry: introducing Geochemical Data Toolkit (GCDkit). *Journal of Petrology* **47**, 1255–9.

Jayananda M, Moyen J-F, Martin H, Peucat J-J, Auvray B and Mahabaleswar B (2000) Late Archaean (2550–2520 Ma) juvenile magmatism in the Eastern Dharwar craton, southern India: constraints from geochronology, Nd–Sr isotopes and whole rock geochemistry. *Precambrian Research* **99**, 225–54.

Kay RW and Kay SM (1993) Delamination and delamination magmatism. *Tectonophysics* **219**, 177–89.

Kelsey DE and Hand M (2015) On ultrahigh temperature crustal metamorphism: phase equilibria, trace element thermometry, bulk composition, heat sources, timescales and tectonic settings. *Geoscience Frontiers* **6**, 311–56.

Kemp AIS, Shimura T and Hawkesworth CJ (2007) Linking granulites, silicic magmatism, and crustal growth in arcs: ion microprobe (zircon) U-Pb ages from the Hidaka metamorphic belt, Japan. *Geology* **35**, 807–10.

Khalaf EA, Khalaf M and Oraby F (2011) Polybaric evolution of the volcanic rocks at Gabal Nuqara, North Eastern Desert, Egypt. In *Topics in Igneous Petrology* (eds J Ray, G Sen and B Ghosh), pp. 277–317. Dordrecht: Springer.

Klaver M, De Roever EW, Thijssen AC, Bleeker W, Söderlund U, Chamberlain K, Ernst R, Berndt J and Zeh A (2016) Mafic magmatism in the Bakhuis Granulite Belt (western Suriname): relationship with charnockite magmatism and UHT metamorphism. *GFF* **138**, 203–18.

Kohn MJ, Engi M and Lanari P (2017) Petrochronology. *Methods and Applications, Mineralogical Society of America Reviews in Mineralogy and Geochemistry* **83**, 575.

Kröner A, Santosh M, Hegner E, Shaji E, Geng H, Wong J and Xie H (2015) Palaeoproterozoic ancestry of Pan-African high-grade granitoids in southernmost India: implications for Gondwana reconstructions. *Gondwana Research* **27**, 1–37.

Kumar TV, Rao YB, Plavsa D, Collins AS, Tomson JK, Gopal BV and Babu EVSSK (2017) Zircon U-Pb ages and Hf isotopic systematics of charnockite gneisses from the Ediacaran–Cambrian high-grade metamorphic terranes, southern India: constraints on crust formation, recycling, and Gondwana correlations. *Geological Society of America Bulletin* **129**, 625–48.

Ludwig KR (2012) *ISOPLOT ver. 4.15*. Berkeley, California: Berkeley Geochronology Center.

McDonough WS (1990) Constraints on the composition of the continental lithospheric mantle. *Earth and Planetary Science Letters* **101**, 1–18.

McKenzie DAN and Bickle MJ (1988) The volume and composition of melt generated by extension of the lithosphere. *Journal of Petrology* **29**, 625–79.

Menzies MA, Kyle PR, Jones M and Ingram G (1991) Enriched and depleted source components for tholeiitic and alkaline lavas from Zuni-Bandera, New Mexico: inferences about intraplate processes and stratified lithosphere. *Journal of Geophysical Research: Solid Earth* **96**, 13645–71.

Mullen ED (1983) $MnO/TiO_2/P_2O_5$: a minor element discriminant for basaltic rocks of oceanic environments and its implications for petrogenesis. *Earth and Planetary Science Letters* **62**, 53–62.

Nandakumar V and Harley SL (2019) Geochemical signatures of mid-crustal melting processes and heat production in a hot orogen: the Kerala Khondalite Belt, Southern India. *Lithos* **324**, 479–500.

Nowell GM, Kempton PD, Noble SR, Fitton JG, Saunders AD, Mahoney JJ and Taylor RN (1998) High precision Hf isotope measurements of MORB and OIB by thermal ionisation mass spectrometry: insights into the depleted mantle. *Chemical Geology* **149**, 211–33.

O'Reilly SY and Griffin WL (2013) Mantle metasomatism. In *Metasomatism and the Chemical Transformation of Rock* (eds DE Harlov and H Austrheim), pp. 471–533. Berlin and Heidelberg: Springer.

Paton C, Hellstrom J, Paul B, Woodhead J and Hergt J (2011) Iolite: freeware for the visualisation and processing of mass spectrometric data. *Journal of Analytical Atomic Spectrometry* **26**, 2508–18.

Pearce JA (2008) Geochemical fingerprinting of oceanic basalts with applications to ophiolite classification and the search for Archean oceanic crust. *Lithos* **100**, 14–48.

Pearce NJ, Perkins WT, Westgate JA, Gorton MP, Jackson SE, Neal CR and Chenery SP (1997) A compilation of new and published major and trace element data for NIST SRM 610 and NIST SRM 612 glass reference materials. *Geostandards Newsletter* **21**, 115–44.

Petrus JA and Kamber BS (2011) VisualAge: a novel approach to U–Pb LA–ICP–MS geochronology. *Mineralogical Magazine* **75**, 1633.

Plavsa D, Collins AS, Foden JF, Kropinski L, Santosh M, Chetty TRK and Clark C (2012) Delineating crustal domains in Peninsular India: age and

chemistry of orthopyroxene-bearing felsic gneisses in the Madurai Block. *Precambrian Research* **198**, 77–93.

Prakash D, Arima M and Mohan A (2007) Ultrahigh-temperature mafic granulites from Panrimalai, south India: constraints from phase equilibria and thermobarometry. *Journal of Asian Earth Sciences* **29**, 41–61.

Ratheesh-Kumar RT, Dharmapriya PL, Windley BF, Xiao WJ and Jeevan U (2020) The tectonic "umbilical cord" linking India and Sri Lanka and the tale of their failed rift. *Journal of Geophysical Research: Solid Earth* **125**, e2019JB018225.

Ray S, Tiwari AK and Sarkar T (2021) Ultrahigh-temperature mafic granulites from the Madurai Block, southern India: constraints from conventional thermobarometry, pseudosection analysis, and rare earth element-based thermometry. *Geological Journal* **56**, 3720–44.

Rollinson HR (2014) *Using Geochemical Data: Evaluation, Presentation, Interpretation*. London: Routledge.

Rubatto D, Chakraborty S and Dasgupta S (2013) Timescales of crustal melting in the Higher Himalayan Crystallines (Sikkim, Eastern Himalaya) inferred from trace element-constrained monazite and zircon chronology. *Contributions to Mineralogy and Petrology* **165**, 349–72.

Rubatto D and Hermann J (2003) Zircon formation during fluid circulation in eclogites (Monviso, Western Alps): implications for Zr and Hf budget in subduction zones. *Geochimica et Cosmochimica Acta* **67**, 2173–87.

Sajna S, Tomson JK, Dev JA, Sorcar N and Kumar TV (2022) Neoproterozoic Mafic Magmatism in Nagercoil Block, Southern India and Its Implications on the Gondwana Collisional Orogeny. *Minerals*, **12**, 1509.

Santos MM, Lana C, Scholz R, Buick I, Schmitz MD, Kamo SL, Gerdes A, Corfu F, Tapster S, Lancaster P and Wiedenbeck M (2017) A new appraisal of Sri Lankan BB zircon as a reference material for LA-ICP-MS U-Pb geochronology and Lu-Hf isotope tracing. *Geostandards and Geoanalytical Research* **41**, 335–58.

Santosh M, Tsunogae T, Malaviarachchi SP, Zhang Z, Ding H, Tang L and Dharmapriya PL (2014) Neoproterozoic crustal evolution in Sri Lanka: insights from petrologic, geochemical and zircon U–Pb and Lu–Hf isotopic data and implications for Gondwana assembly. *Precambrian Research* **255**, 1–29.

Scherer E, Münker C and Mezger K (2001) Calibration of the lutetium-hafnium clock. *Science* **293**, 683–7.

Sláma J, Košler J, Condon DJ, Crowley JL, Gerdes A, Hanchar JM, Horstwood MS, Morris GA, Nasdala L, Norberg N, Schaltegger U and Whitehouse MJ (2008). Plešovice zircon: a new natural reference material for U–Pb and Hf isotopic microanalysis. *Chemical Geology* **249**, 1–35.

Song S, Wang M, Wang C and Niu Y (2015) Magmatism during continental collision, subduction, exhumation and mountain collapse in collisional orogenic belts and continental net growth: a perspective. *Science China Earth Sciences* **58**, 1284–304.

Srinivasan V and Rajeshdurai P (2010) The Suruli shear zone and regional scale folding pattern in Madurai block of Southern Granulite Terrain, south India. *Journal of Earth System Science* **119**, 147–60.

Sun SS and McDonough WF (1989) Chemical and isotopic systematics of oceanic basalts: implications for mantle composition and processes. In *Magmatism in the Ocean Basins* (eds AD Saunders and MJ Norry), pp. 313–45. Geological Society of London, Special Publication no. 42.

Takahashi E and Kushiro I (1983) Melting of a dry peridotite at high pressures and basalt magma genesis. *American Mineralogist* **68**, 859–79.

Takamura Y, Tsunogae T, Santosh M, Malaviarachchi SP and Tsutsumi Y (2015) Petrology and zircon U–Pb geochronology of metagabbro from the Highland Complex, Sri Lanka: implications for the correlation of Gondwana suture zones. *Journal of Asian Earth Sciences* **113**, 826–41.

Takamura Y, Tsunogae T and Tsutsumi Y (2020) U–Pb geochronology and REE geochemistry of zircons in mafic granulites from the Lützow-Holm complex, East Antarctica: implications for the timing and P–T path of post-peak exhumation and Antarctica–Sri Lanka correlation. *Precambrian Research* **348**, 105850.

Tomson JK, Rao YB, Kumar TV and Choudhary AK (2013) Geochemistry and neodymium model ages of Precambrian charnockites, Southern Granulite Terrain, India: constraints on terrain assembly. *Precambrian Research* **227**, 295–315.

Wang B, Wei CJ, Tian W and Fu B (2020) UHT metamorphism peaking above 1100° C with slow cooling: insights from pelitic granulites in the Jining complex, North China Craton. *Journal of Petrology* **61**, egaa070.

Wang M, Wang CY and Sun Y (2013) Mantle source, magma differentiation and sulfide saturation of the ~637 Ma Zhouan mafic–ultramafic intrusion in the northern margin of the Yangtze Block, Central China. *Precambrian Research*, **228**, 206–22.

Wedepohl KH (1995) The composition of the continental crust. *Geochimica et Cosmochimica Acta* **59**, 1217–32.

Wilson M (1989) *Igneous Petrogenesis*. London: Unwin Hyman, 466 pp.

Yang QY, Ganguly S, Shaji E, Dong Y and Nanda-Kumar V (2019) Extensional collapse of the Gondwana orogen: evidence from Cambrian mafic magmatism in the Trivandrum Block, southern India. *Geoscience Frontiers* **10**, 263–84.

Zeh A, Gerdes A, Klemd R and Barton Jr JM (2008) U–Pb and Lu–Hf isotope record of detrital zircon grains from the Limpopo Belt: evidence for crustal recycling at the Hadean to early-Archean transition. *Geochimica et Cosmochimica Acta* **72**, 5304–29.

Zhao JH and Zhou MF (2007) Geochemistry of Neoproterozoic mafic intrusions in the Panzhihua district (Sichuan Province, SW China): implications for subduction-related metasomatism in the upper mantle. *Precambrian Research* **152**, 27–47.

https://doi.org/10.1017/S0016756823000079 Published online by Cambridge University Press